3-9-2021

Complex Fluid Dynamics: Chemo-Hydrodynamics Driven by Autocatalytic Reaction Fronts

Matthew Walter Eskew
Portland State University

Complex Fluid Dynamics: Chemo-Hydrodynamics Driven by Autocatalytic Reaction Fronts

by

Matthew Walter Eskew

A thesis submitted in partial fulfillment of the
requirements for the degree of

Master of Science
in
Chemistry

Thesis Committee:
Albert S. Benight, Chair
Dean Atkinson
Erik Bodegom

Portland State University
2021

ABSTRACT

Chemo-hydrodynamics generated from reaction-diffusion-convection processes of autocatalytic chemical systems are extensively studied for their applications in modeling complex systems. Compared to the more extensively studied autocatalytic systems, chlorite-tetrathionate and chlorite-trithionate, the chlorite-thiourea systems is relatively unexplored. Compared to the two previous systems, chlorite-thiourea has more straightforward chemical kinetics. To narrow the gap between chlorite-thiourea and the other systems a combination of experimental study and numerical simulation were employed to quantify this system.

Compared to established literature, experiments were performed at five orders of magnitude lower concentration of indicator, minimizing confounding effects of indicator on hydrodynamic motion. To accurately image the system, self-written MATLAB code was employed to enhance the color spectrum of experimental videos and images. A combination of two pH indicators was used to effectively isolate the wave front of the reaction system allowing for velocity measurements.

Utilizing experimental data, a simplified kinetics model was generated and a theoretical reaction rate constant was determined for the simplified model using a one-dimensional reaction diffusion solver written in MATLAB. The resulting rate constant of 3.6×10^5 $M^{-2.5}s^{-1}$ was then used to construct a two-dimensional numerical simulation in COMSOL 5.3a. This model was used to test validity of using the Boussinesq Approximation to treat these autocatalytic systems as incompressible rather than as compressible fluids.

Numerical simulations generated in COMSOL were able to accurately recreate chemo-hydrodynamic behaviors and wave velocities as measured experimentally. No detectable difference in results were determined between solving the system as in-

compressible with the Boussinesq Approximation compared to solving the full Navier-Stokes equations. However, there was a 20% time savings in solving the full Navier-Stokes equation compared to the simplified version. This result showed that when modeling these systems, computational efficiency was not saved by using the Boussinesq approximation. While these results were not different, larger or more complex systems may benefit from a full treatment of the Navier-Stokes equations rather than an approximation.

I dedicate this thesis to my family and friends.

ACKNOWLEDGEMENTS

I want to first thank my family (Rod and Concetta Higgins, Carl and Lauren Berry, Jay Sanders, Scott Watson) that provided financial support in taking post-baccalaureate courses that enabled me to enroll in the PhD program at Portland State. Without their help I would probably not have written this thesis. Also, thanks to Teetee Diane for getting me a plane ticket back from the chemical chaos conference in Boston, otherwise I might still be in Boston, and thankfully I am not Rita, who you said you would have left stranded.

A special thanks to my lovely wife Rita for supporting me through this program and inspiring me to be better. Her love and support was especially important in being able to persevere and complete not only this MS work but also a PhD.

Finishing this would not be possible without support from Professor Albert Benight who agreed to step-in and advise me. I know this material is outside of his area of interest, but he provided valuable support and insight.

I had a strong start in the PhD program thanks to the advice and support of Dr. Kudzanai Chipiso and Dr. Wilbes Mbiya. Both are absolutely wonderful people and exemplary scientists. Their mentorship is truly appreciated. Likewise, it was an honor to mentor and work with a number of undergraduate scientists who have gone on to great careers (and some to graduate school). These include Isabelle Logan, John Winner, Astrid Woodall, and Megan Kight.

Thanks as well to my current committee members, Professor Dean Atkinson and Professor Erik Bodegom and to past committee members. Likewise, a thank you to Dr. John Ramshaw of Livermore National Laboratory who provided a number of valuable references and keen insight into this project.

Lastly, I want to thank my friend, collaborator, and co-founder of Thursday

Gentleman's Club (even when it fell on days other than Thursday), Dr. Luke Lutkus.

Life is a storm, my young friend. You will bask in the sunlight one moment, be shattered on the rocks the next. What makes you a man is what you do when that storm comes. You must look into that storm and shout as you did in Rome. Do your worst, for I will do mine! Then the fates will know you as we know you

Alexandre Dumas

TABLE OF CONTENTS

LIST OF TABLES

LIST OF FIGURES

LIST OF PHYSICAL CONSTANTS

Boltzmann's Constant	k_B	1.3806485 x 10^{-23} J K^{-1}
Density of H_2O	ρ_{H_2O}	1 g cm^{-1}
Gravitational Acceleration constant	g	980.67 cm s^{-2}
Kinematic Viscosity of H_2O	ν_{H_2O}	$0.893x10^{-6}$ m^2 s^{-1} or Stokes
Thermal Expansion Coefficient of H_2O	β_{H_2O}	-0.4 kg m^{-3} K^{-1}
Universal Gas Constant	R	8.314 J mol^{-1} k^{-1}
Viscosity of H_2O	μ_{H_2O}	1 centipoise (10^{-3} Pa s)

LIST OF SYMBOLS

c	Concentration	mole (mol)
C_p	Specific Heat Capacity at constant pressure	J kg^{-1} K^{-1}
D_j	Diffusion Coefficient of species j	m^2 s^{-1}
D_j^T	Thermal Diffusion Coefficient of species j	kg m^{-1} s^{-1}
E	Energy Density	erg J cm^{-3}
H_{rxn}	Enthalpy of Reaction	kJ mol^{-1}
I	Total Number of Chemical Reactions	
i	Index for Chemical Reactions	
j	Index for Chemical Species	
k_f	Forward Reaction Rate Constant	Depends on reaction order
k_r	Reverse Reaction Rate Constant	Depends on reaction order
K	Total Number of Chemical Species	
m_j	Mass of Species j	grams
n_j	Number Density of Species j	cm^{-3}
N	Total Number Density	cm^{-3}
p	Pressure	Pascal (Pa) or kg $m^{-1}s^{-1}$
Q	Heat	Joule (J)
q_i	Progress of Reaction i	mol m^{-3} s^{-1}
t	time	seconds (s) or minutes (min)
T	Temperature	Kelvin (K)
v	Fluid Velocity	cm s^{-1}
V	Volume	cm^{-3}

α	Thermal Diffusivity	$m^2\ s^{-1}$
β	Thermal Expansion Coefficient	K^{-1}
λ	Thermal Conductivity Coefficient	watts $m^{-1}\ K^{-1}$
μ	Viscosity	g $cm^{-1}\ s^{-1}$ (Poise)
ν	Kinematic Viscosity	$cm^2\ s^{-1}$ (Stokes)
ξ	Extent of Reaction	mol
ρ	Density	g cm^{-1}
σ	Surface Tension	N m^{-2}
ω	Angular Velocity	$rad\ s^{-1}$
∇	Gradient	
$\dot{\omega}_j$	Net rate of production	mol $m^{-3}\ s^{-1}$

CHAPTER 1
BACKGROUND

1.1 Motivation:

Reaction-Diffusion-Convection (RDC) systems can be used to drive hydrodynamic motion through diffusion, buoyancy, or thermocapillary effects. The study of these systems using autocatalytic reactions as a driving force, has been relatively limited and clustered around a few specific reactions of chlorite with sulfur compounds. In comparison to the widely studied chlorite-tetrathionate and chlorite-trithionate systems there has been relatively fewer investigations on hydrodynamics driven by the reactions of chlorite with thiourea.[1–6] This provides an ideal experimental platform to challenge assumptions and approximations historically used in modeling and analyzing these systems.

A key element of these reactions is that they are driven by an acid wave front; thus making it convenient to visualize the waves using pH indicators. Historically, indicators have been used at relatively high concentrations and shown to effect both hydrodynamic motion, by changing surface tension of the solution, and reaction kinetics by acting as a buffer.[1,7] Inestigating effects of using significantly lower concentrations of pH indicators on hydrodynamics is a key aim of this study as described in Section 1.3 and Chapter 2.

Unlike the chlorite-tetrathionate and chlorite-trithionate systems, there has not been numerical simulations of hydrodynamic behaviors generated by the chlorite-thiourea system. To address this shortcoming, a numerical simulation was created and demonstrated in Chapter 2. Simulations for tetrathionate and trithionate sys-

tems provided a basic outline for modeling. Initially a simplified chemical model was generated and tested as a one-dimensional reaction-diffusion simulation to determine the reaction rate constant for the simplified model. This was done using MATLAB as described in Section 2.3.2. For two-dimensional models, examples in the literature utilize several simplifying approximations and assumptions; some that may not be valid for physical systems. Specifically, the Boussinesq Approximation assumes a fluid is incompressible and density changes only effect buoyant forces.[8] However, evidence exists that under conditions similar to those displayed in autocatalytic reaction systems, the Boussinesq Approximation was invalid.[9,10] Contrasting with established literature precedent a numerical simulation was proposed in Section 1.2.8 that does not invoke simplifications regarding the Boussinesq Approximation. Results of hydrodynamic simulations of the chlorite-thiourea system utilizing the new approach and Boussinesq Approximation are presented in Section 2.3.3

Results of this thesis work provide a new basis for utilization of pH indicators for studying hydrodynamics driven by autocatalytic reaction systems. Applying self-written MATLAB code for image enhancement allowed for the use of significantly less indicator in order to visualize hydrodynamic behaviors of these systems. Also, advances in computing power enabled solving numerical simulations of complex fluid dynamics without requiring the use of simplifying approximations.

1.2 Fluid Dynamics

At its most basic level, fluid dynamics is the study of how the variety of complex flow patterns of liquids and gases manifest in physical ways. Fluid dynamics is a long studied multidisciplinary field of science that includes physics, engineering, and mathematics. Fluid phenomena can involve studies on the molecular to macroscopic levels. However, most flows can be understood and detailed purely from a macroscopic

perspective without connecting to the microscopic structure of the fluid.[11]

1.2.1 History

History of the study of fluid dynamics dates back to at least 250 B.C. when Archimedes wrote *On Floating Bodies*. That book introduced basic concepts of fluid pressure and hydrostatics. It also took an additional 18 centuries before his work was continued by the likes of Galileo.[12] A side effect of Archimedes' work is that it led to an early form of differential calculus. It was also during this time that Hero of Alexandria worked extensively on hydrostatics developing Hero's fountain and the earliest example of force pumps.[13] The work by these two men serve as some of the earliest examples of applied fluid dynamics.

There was a great lag in theoretical work after the time of Archimedes and Hero until the 17^{th} to 19^{th} centuries. In the preceding time, most of the advancements came from engineering feats and improved designs, such as canals, ships, and aqueducts, rather than from detailed analysis. The 17^{th} to 19^{th} centuries were a time rife with great experimentalists like Leonardo Da Vinci, who captured accurate descriptions of many fluid phenomena in his notes. However, there was a disconnect with theoreticians at the time; Isaac Newton and Daniel Bernoulli, among others, developed many equations of motions to explain a variety of frictionless flows. Their elegant equations were ignored due to having limited real world applications, i.e., engineering systems. It was not until the end of the 19^{th} century that experimentalists were able to verify earlier theories regarding fluid motion.

This era produced some of the best known names in fluid dynamics including; Lord Rayleigh, Claude-Louis Navier, George Stokes, Osbourne Reynolds, and Ludwig Prandtl. Lord Rayleigh proposed dimensional analysis to study fluid flows.[15] While Osbourne Reynolds conducted pipe flow experiments; the Dimensionless Reynolds

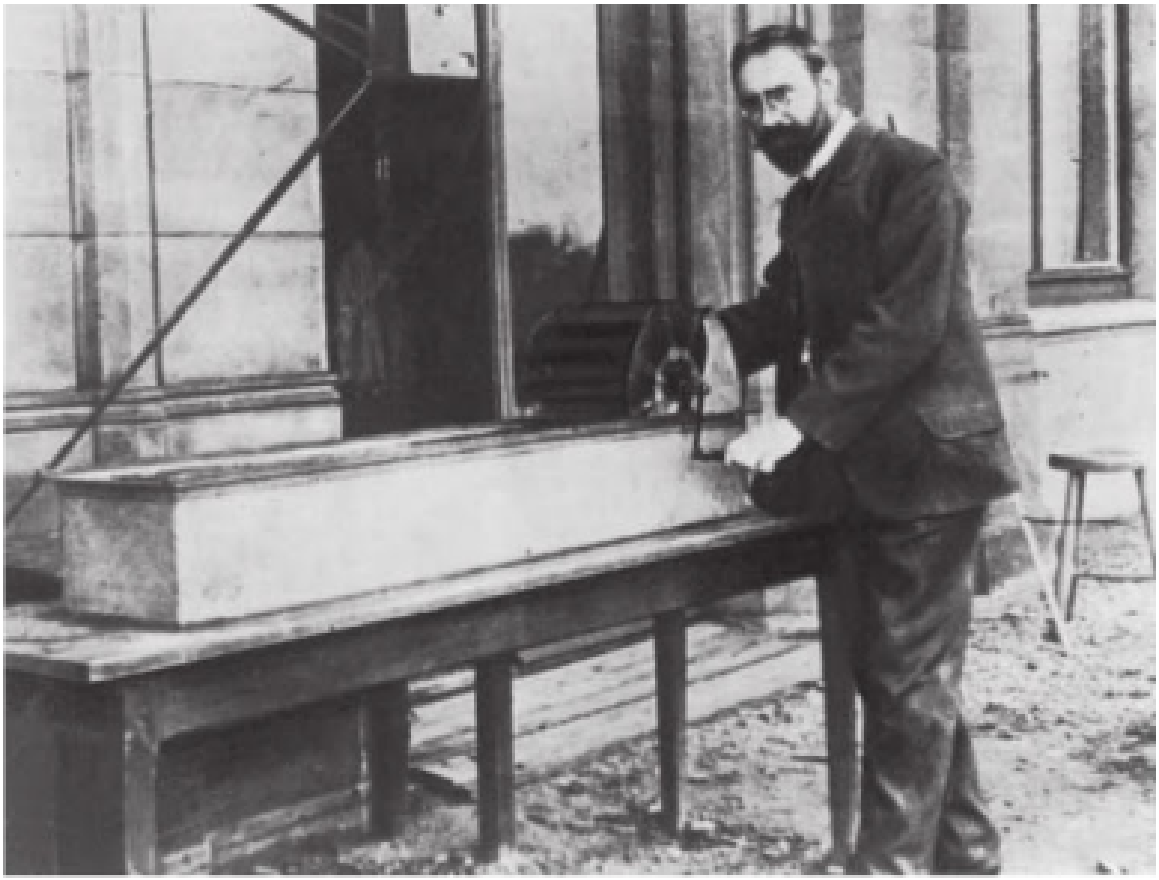

Figure 1.1: Ludwig Prandtl and his flow visualization set-up, 1904.[14]

Number is named after him. Navier and Stokes were able to include viscous terms into Newtonian equations of motion ultimately leading to the Navier-Stokes equations.[16] At the time these equations were too difficult to solve analytically for all but the simplest laminar flows.

In 1904 Ludwig Prandtl published one of the most important papers of modern fluid dynamics. In this work Prandtl showed both experimentally and theoretically existence of a boundary layer in a fluid flow where both the Euler and Bernoulli equations apply.[17] This boundary layer theory served as a key foundation of modern fluid dynamics.[18,19] Ludwig Prandtl is shown with his experimental apparatus in Figure 1.1.

1.2.2 Theoretical Background

In developing a model for a fluid dynamics system it is important to understand the differences between the system and the control volume. The system comprises the entire mass of fluid being studied. It is, however, impractical to follow and model the physical and chemical processes within the system as a whole. Instead, a Eulerian control volume is used. This is a volume in a fixed region of space.[20]

Momentum, mass, energy, chemical species may be transported both in and out of a control volume. In practice, control volumes are defined by parameters and refinement of the mesh used in creating the model.[21] In a triangular mesh utilized in Section 2.3.3, each triangular portion is a unique control volume. A reasonable fluid dynamical model should attempt to establish a relationship between extensive properties defined by their time rates of change, and subsequent behavior of intensive properties within a control volume. These intensive properties provide a snapshot in time.

1.2.3 Conservation Laws and the Continuity Equation

Conservation laws require that extensive properties of a fluid dynamical system obey the first law of thermodynamics (conservation of energy) and conservation of mass. In reactive flows, chemical reactions can cause mass changes as reactive species are converted to products and with energy released or absorbed depending on the reaction.

Mass flux in closed systems is zero, i.e. mass is conserved.[20] In practice, the continuity equation describes conservation of mass in a fluid system.

The control volume (V), is an arbitrary fixed volume, as represented in Figure 1.2. Fluid can move in or out at any point on the surface of the control volume. Presumably, no part of the control volume resides along a boundary.

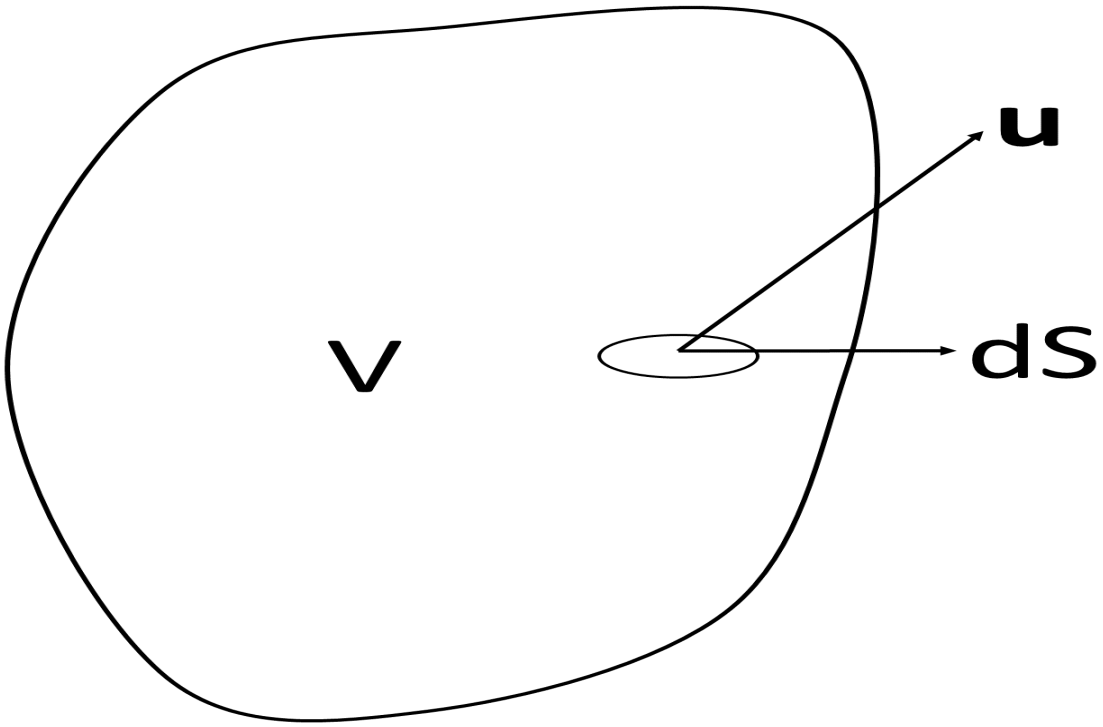

Figure 1.2: Derivation of the continuity equation.

In Figure 1.2, dS is an arbitrarily determined area on the surface of the fluid volume and **u** is the density flux of that area. If **u** is positioned so as to transfer fluid out of V, mass flux results. The mass flux depends on the fluid density where,

$$\text{Mass in V} = \int_V \rho dV \tag{1.1}$$

and the

$$\text{Mass Flux} = \int_S \rho \mathbf{u} \bullet dS \tag{1.2}$$

Then the total mass of the control volume is given by,[11]

$$\text{Total Mass in V} = \int_V \frac{\partial \rho}{\partial t} dV + \int_S \rho \mathbf{u} \bullet dS \tag{1.3}$$

These equations apply to a fluid particle of definite volume. It is often more useful to know the mass balance at a single point. To achieve this, Equation 1.3 is integrated for an infinitesimally small volume, viz

$$\frac{\partial \rho}{\partial t} = - \lim_{V \to 0} \left[\int \rho \mathbf{u} \bullet \frac{dS}{V} \right] \tag{1.4}$$

Equation 1.4 refers to a point within the arbitrary fluid volume. Thus, both $\mathbf{u}$ and ρ are functions of position in the volume. The gradient operator (∇) is the extent to which a point in the vector field acts as a source or sink.[22] By utilizing the gradient operator, Equation 1.4 becomes[11,23]

$$\frac{\partial \rho}{\partial t} = -\nabla \bullet \rho \mathbf{u} \tag{1.5}$$

Which is the continuity equation for mass conservation, i.e.

$$\frac{\partial \rho}{\partial t} + \nabla \bullet (\rho \mathbf{u}) = 0 \tag{1.6}$$

In a fluid where density is constant over time, $\frac{\partial \rho}{\partial t} = 0$ and Equations 1.5 and 1.6 reduce to the much simpler form,

$$\nabla \bullet \mathbf{u} = 0 \tag{1.7}$$

Beginning with the continuity equation, four major components contribute to development of a complete model; chemical, thermal, physical, and boundary.

1.2.4 Chemical Processes

In general a chemical reaction can be represented as,

$$\mathrm{aA} + \mathrm{bB} \longrightarrow \mathrm{cC} \tag{R 1.1}$$

a moles of A react with b moles of B to produce c moles of C. Rate equations can be written for consumption of A and B, and production of C. For example,

$$-\frac{dA}{dt} = k[A]^a[B]^b \tag{1.8}$$

A system of reactions can be treated as the sum of individual reactions as,

$$\sum_{j=1}^{K} \nu_{j,i}^{'} X_j \rightleftharpoons \sum_{j=1}^{K} \nu_{j,i}^{"} X_j \quad i = (1, 2, 3, ...I) \tag{1.9}$$

where X_j is the chemical species, K is the total number of species, and j is the counting variable for the individual species. $\nu^{'}$ and $\nu^{"}$ represent the forward and reverse stoichiometric coefficients respectively of species j. To index the reactions the variable i is used with I being the total number of reactions in the proposed mechanism.

As a corollary to Equation 1.9 using the same nomenclature it is possible to derive an equation for the rates of individual reactions in the system, i.e. extent of reaction is

$$q_i = k_{f,i} \prod_{j=1}^{K} [X_j]^{v_{j,i}^{'}} - k_{r,i} \prod_{j=1}^{K} [X_j]^{v_{j,i}^{"}} \tag{1.10}$$

$k_{f,i}$ and $k_{r,i}$ in Equation 1.10 are the forward and reverse reaction rates, respectively. This generalized form gives the time dependence of the concentration for

each species, where

$$\frac{\partial X_j}{\partial t} = \sum_{i}^{I} \nu_{i,j} q_i \tag{1.11}$$

Equation 1.11, when properly parameterized with results from experiments provides a scaffold for describing interactions of chemical reactions in fluid dynamic models.

The chlorite system of oscillators was one of the first systematically designed chemical oscillators birthed from research into the Belousov–Zhabotinsky reaction. Discovery of the first chlorite based oscillator led to development of whole families of these oscillators using a variety of substrates.[24] The chlorite-thiourea reaction was one such system. The kinetics for this reaction have been determined both experimentally and mechanistically.[25–27]

Experiments described in Chapter 2 reveal that a full accounting of individual reactions was not required to explain observed hydrodynamic behavior. Reactions of chlorite and sulfur compounds are controlled by the chlorite side of the reaction and the ratio between chlorite and thiourea. A simplified chemical model was used to account for overall stoichiometry and focus on the ClO_2^-, $SC(NH_2)_2$, and H^+ species. This approach was validated in specific simulations for the chlorite-tetrathionate systems.[3,4,6,28–30]

The critical reactions begin with the initial oxidation of thiourea by chlorite to form aminomethanesulfonic acid, $HO_3SC(NH)NH_2$ (AMSA), hypochlorous acid, HOCl, acid, H^+, and free chloride, Cl^-[25], i.e.

$$3\,ClO_2^- + 2\,SC(NH_2)_2 \xrightarrow{k_f} 2\,HO_3SC(NH)NH_2 + 2\,Cl^- \tag{R 1.2}$$

This initial reaction, R 1.2, proceeds slowly with a $K_f = 10$. Excess chlorite

further oxidizes AMSA to form inorganic products of sulfate, chloride, and acid[25], K_f = 5x10^3 s^{-1}, i.e.

$$ClO_2^- + 2\,HO_3SC(NH)NH_2 + 2\,H_2O \xrightarrow{k_f} 2\,SO_4^{2-} + 2\,OC(NH_2)_2 + Cl^- + 4\,H^+ \quad \text{(R 1.3)}$$

The combination of reactions R 1.2 and R 1.3 above provides the ideal stoichiometry based on favorable thermodynamics.[26] For the chlorite-thiourea,[26]

$$2\,ClO_2^- + SC(NH_2)_2 + H_2O \xrightarrow{k_f} SO_4^{2-} + OC(NH_2)_2 + Cl^- + 2\,H^+ \quad \text{(R 1.4)}$$

Experiments could not confirm the proposed stoichiometry in R 1.4.[26] But it should be noted that the conjectured traveling wave front is second order with acid.[25,31] From the balanced chemical reaction in R 1.4, the effective rate law for the alledged traveling acid wave front can be written down from the balanced chemical equation. This rate law is of the same form as that for chlorite-tetrathionate system.[2–4,6]

$$\dot{\omega_j} = k_f[ClO_2^-][SC(NH_2)_2]^{1/2}[H^+]^2 \quad (1.12)$$

$\dot{\omega_j}$ in Equation 1.12, represents *the net rate of production of species j.* The reaction rate constant, k_f, of the simplified chlorite-thiourea model is required to accurately simulate this system. The rest of the physical processes that govern the system are controlled by the kinetics. This is especially true if heat is also generated from the reaction.

Thermal Energy

The chlorite-thiourea system is highly exothermic with a reaction enthalpy (ΔH_{rxn} = -1,170 kJ/mol determined by the sum of the individual reaction steps summarized in R 1.2-R 1.4 (Hess's Law).[32,33] In effect, heat generation accompanies acid production.[1,3,4,28–30]

The stoichiometry and net rate of production of the autocatalytic species (H^+) are coupled to the reaction enthalpy to give temperature changes as a function of time. That is,

$$\frac{\partial T}{\partial t} = |\Delta H_{rxn}| \sum_j \dot{\omega}_j \nu_j \tag{1.13}$$

Equation 1.13 is the net rate of temperature change determined by the reaction rate, $\dot{\omega}_j$, stoichiometric coefficients, ν_j, and reaction enthalpy, ΔH_{rxn}. Note, this is the theoretical temperature change. The actual temperature change depends on the heat capacity of the specific reaction medium. In this case

$$\frac{\partial T}{\partial t} = \frac{|H_{rxn}|}{\rho C_p} \dot{\omega}_j \nu_j \tag{1.14}$$

where the density, ρ, and heat capacity at constant pressure, C_p, of the reaction medium reports on temperature production as a function of time in a particular reaction medium.

1.2.5 Transport Processes

Transport of the fluid system is driven by the chemical processes described above. Three transport processes are considered: diffusion, convection, and momentum.

Diffusion

Diffusion is described in the context of Einstein's classical theory of Brownian motion; concerned with the random diffusion of solute particles in a solvent.[34] At the molecular level, each solute molecule engages in a "random walk", where particles move in an essentially random manner.[35] However, in the presence of a gradient (concentration, temperature, or energy) particle motion is driven directionally by diffusion.

Batchelor and Schurr expanded Einstein's work and defined the mathematical basis for Fick's Laws that are fundamental equations describing mass transport through diffusion.[36–38] Fick's First Law is,

$$J = -D\frac{\partial c}{\partial x} \tag{1.15}$$

where J is the flux, D is the diffusion coefficient, and $\frac{\partial c}{\partial x}$ is the concentration gradient. Diffusion considerations only apply to dilute systems. Diffusion driven reactions are governed by chemical kinetics through Fick's second law,[1,4]

$$\frac{\partial c}{\partial t} + \mathbf{u} \bullet \nabla c = D\nabla^2 c + f(c) \tag{1.16}$$

where the $D\nabla^2 c$ term represents diffusion of a chemical species in three dimensions. The ∇^2 is the Laplacian. $\frac{\partial c}{\partial t}$ is the rate of change of the concentration with time and $\mathbf{u} \bullet \nabla c$ is the projection of the velocity, $\mathbf{u}$, on the concentration gradient. $f(c)$ represents the kinetics of the driving chemical reaction.

Thermal Diffusion

Convection is the production and transport of thermal energy. Transport of thermal energy is governed by the convection-diffusion equation,[4,39]

$$\rho_0 C_p \left[\frac{\partial T}{\partial t} + \mathbf{u} \bullet \nabla T \right] = \kappa_T \nabla^2 T + |\Delta H_{rxn}| f(c) - \alpha(T - T_0) \tag{1.17}$$

where production of thermal energy, $\frac{\partial T}{\partial t}$ arises from the temperature gradient induced by the chemical reaction. The rate of thermal energy production and the temperature gradient formed depends on the specific heat of the system, C_p. The $\kappa_T \nabla^2 T$ term, on the right side of 1.17, is the 3-D diffusion of heat with κ_T the thermal conductivity coefficient. The rate of heat generation is determined by the chemical kinetics and the enthalpy of reaction, i.e. $|\Delta H_{rxn}| f(c)$. α is the thermal diffusivity coefficient. $\alpha(T - T_0)$, accounts for thermal diffusion between warmer product and cooler reactant solutions.

1.2.6 Navier-Stokes Equations

Claude-Louis Navier first applied Newton's second law of motion to analyze fluid dynamics.[40] However, his results were only applied to inviscid flows, with little applicability to real physical systems. Navier's original equation,

$$\rho \frac{D\mathbf{u}}{Dt} = -\nabla \bullet p + \mu \nabla^2 \mathbf{u} + F \tag{1.18}$$

where $\nabla \bullet p$ is the pressure gradient, μ the viscosity, and F the contribution of external forces, such as gravity. George Stokes included viscosity terms in Navier's equations providing the classical Navier-Stokes equation,[11,16] Equation 1.18 can be

rewritten in terms of density to produce[11,41]

$$\frac{\partial \mathbf{u}}{\partial t} + \mathbf{u} \bullet \nabla \mathbf{u} = -\frac{1}{\rho}\nabla p + \nu \nabla^2 \mathbf{u} + \frac{1}{\rho} F \tag{1.19}$$

ν in Equation 1.19 is the kinematic viscosity of the solution defined as μ/ρ. The Navier-Stokes equation (1.19) is the starting point for mathematical descriptions of fluid transport phenomena. The external forces are included as (F) making it possible to account for factors effecting the flow, such as temperature and chemical reactions.[11,16,20,23,42,43]

1.2.7 Boundary Conditions

No Slip & No Flux

The simplest boundaries are no-slip and no-flux. For no-slip boundary conditions there is no fluid movement along the boundary. This is expressed mathematically as:

$$\frac{\partial \mathbf{u}}{\partial x} = 0 \quad \text{at } x = 0, x = L_x \tag{1.20}$$

$$\frac{\partial \mathbf{u}}{\partial z} = 0 \quad \text{at } z = 0 \tag{1.21}$$

For a two-dimensional model there are four boundaries, the three walls and the free surface. Equations 1.20 & 1.21 represent no movement along the walls of the Hele-Shaw cell. The no-flux boundary condition states there is no diffusion of species through the boundary. That is,

$$\frac{\partial c}{\partial x} = 0 \quad \text{at } x = 0, x = L_x \tag{1.22}$$

and

$$\frac{\partial c}{\partial z} = 0 \quad \text{at } z = 0, x = L_z \tag{1.23}$$

The Marangoni Boundary

For a free surface, forces acting on the fluid are governed predominately by surface tension. Surface tension depends on the concentration and temperature, i.e. σ(c,T).

$$d\sigma(c,T) = \frac{\partial \sigma}{\partial T} dT + \frac{\partial \sigma}{\partial c} dc \tag{1.24}$$

Based on effects of viscosity and surface tension, both temperature and concentration induce gradients in the horizontal velocity at the free surface . That is,

$$\mu \frac{\partial \mathbf{u}}{\partial z}\bigg|_{z \to L_z} = \frac{\partial \sigma}{\partial x} = \frac{\partial \sigma}{\partial T}\frac{\partial T}{\partial x} + \frac{\partial \sigma}{\partial c}\frac{\partial c}{\partial x} \tag{1.25}$$

Flow velocity induced by surface tension changes, only holds true at the free surface, z = L_z, with diminishing effects further from the free surface.

1.2.8 New Approach versus Standard Methodology

Standard Methodology

A system of four primary equations forms the core for modeling using the standard approach. First, density changes are not considered in the continuity equation and the system is assumed to be incompressible, i.e.[1,4,30]

$$\nabla \bullet \mathbf{u} = 0 \tag{1.26}$$

Generally in a dilute system, density changes over time are small enough to

be neglected. This assumption enables use of the Boussinesq approximation. The Boussinesq approximation ignores density changes except when effected by gravity. This is the case for buoyancy driven flows. The Boussinessq approximation in a reactive flow simplifies to:

$$\rho = \rho_0(1 - \alpha(T - T_0) + \sum \beta_i(c - c_0)) \tag{1.27}$$

with:

$$\alpha = -\left(\frac{1}{\rho}\right)\frac{\partial \rho}{\partial T} \qquad \beta = \left(\frac{1}{\rho}\right)\frac{\partial \rho}{\partial c_i} \tag{1.28}$$

The subscript '0' denotes initial conditions. α is the thermal expansion coefficient and β is the isothermal expansion coefficient. Thus density changes are a linear function of both concentration and temperature.[4] The Boussinesq approximation, Equation 1.27, is then inserted into Darcy's Law.

Darcy's law describes the flow of a fluid through a porous layer as a function of density and viscosity most often used in Brinkman form to describe flows through boundaries, viz[7,44,45]

$$\nabla \rho = -\frac{\mu}{\kappa}u + \rho(c, T)g \tag{1.29}$$

$\rho(c, T)g$ in Equation 1.29 is the density as a function of concentration (c) and temperature (T) multiplied by gravity. This is a limiting case of the Boussinesq approximation. μ and κ are viscosity of the fluid and permeability of the medium, respectively.

For an incompressible fluid a set of partial differential equations are generated, which allows for modeling of the spatio-temporal dynamics. The Boussinesq approximation allows for solution of convective flow without having to utilize the compressible Navier-Stokes equations.[46] The Boussinesq approximation has been used for

many years because of computational limitations present in creation of early models. However, the Boussinesq approximation is only accurate when temperature changes of water are below 2 degrees (with a variance of less than 1%).[9,42] Errors grow rapidly with larger temperature differences. In the chlorite-thiourea system the temperature changes averages 3 degrees.

Our Approach

Our aim was to develop a general model without assuming incompressibility. In this case, the full continuity equation was used.

$$\frac{D\rho}{Dt} + \nabla \bullet (\rho u) = 0 \tag{1.30}$$

Assuming (using the Boussinesq approximation) that density changes are the only source of buoyant forces, density gradients have no impact on the other fluid flow parameters (i.e. momentum, convection, etc). Alternatively, use of the full continuity equation considers density changes for each control volume comprising the entire density gradient. This provides a more complete view of the fluid dynamic system with all density changes accounted for and accurately applied to the momentum terms of the Navier-Stokes equations.

Computational capabilities have grown at an exponential rate, predicted by Moore's law.[47] The speed of the processors are scaled in terms of floating operations per second (FLOPS). With the rate of growth of computational power, desktop workstations now have capabilities that were only available at national research laboratories with supercomputers 20 years ago; thus enabling simulations without the use of a super-computing cluster. Benchmarks had the most powerful supercomputer, the ASCI Red, rated at 2 teraflops by the end of its operational lifespan in 2005.[48] Current Knights Landing processors from Intel are rated at six teraflops of single

precision accuracy per chip.[49] This provides 3x the processing power of a ~20 year old supercomputer in a desktop workstation. Numerical simulation software is now able to be run on a desktop that would previously require a supercomputer.

With increased computational power it is not necessary to invoke the Boussinesq approximation. Better computers also makes it possible now to test the accuracy and efficiency of the Boussinesq approximation.

1.2.9 Hydrodynamic Motion

Exothermic autocatalytic reactions have been found to supply and maintain a temperature difference, ΔT, at the wavefront of hydrodynamic instabilities.[50] This allows for a chemical reaction to drive hydrodynamic motion. These convective flows can be due to thermocapillary (Marangoni-type) convection coupled to Rayleigh-Taylor, Rayleigh-Bénard, or double diffusive types of hydrodynamic flows. Each can be triggered by spatial temperature and concentration gradients.[51,52]

With an exothermic chemical reaction in an aqueous environment, free convection can deform the interface between reactants and products by producing density inhomogeneities in the reaction medium. This effect is exaggerated in the chlorite-thiourea reaction because the products, sulfate and chloride are dense and ionic. Meanwhile, the reactants contain a light organic molecule. Convection allows this relationship to invert, allowing products to temporarily become less dense than reactants until thermal equilibrium is attained.[53]

When a dense solution overlies a less dense one, due to convection, the resulting front is unstable. In this case any deformity in the density front will grow. Deformities in these types of fronts are known as Rayleigh-Taylor instabilities, where a more dense solution sinks into a rising less dense solution. This behavior can be visualized as density fingering or thermal plumes.

Changes in temperature, density, viscosity, surface tension, and/or chemical composition are capable of triggering convective motions.[30] Convection, is used to describe interpenetration and spatial motion of fluid particles and how compressive forces can change the density. Within the chlorite-thiourea system, Marangoni and double diffusive convection have the largest impact and lead to the hydrodynamic behaviors shown in Figure 1.3, over five minutes.

Marangoni convection is driven by changes in temperature or chemical composition that cause changes in surface tension; Marangoni convection is also referred to as thermocapillary convection. A classic example of this process is the "Tears of wine", where streaks of wine will climb the side of a wine glass. This is caused by a local change in composition causing changes in surface tension gradients.[54]

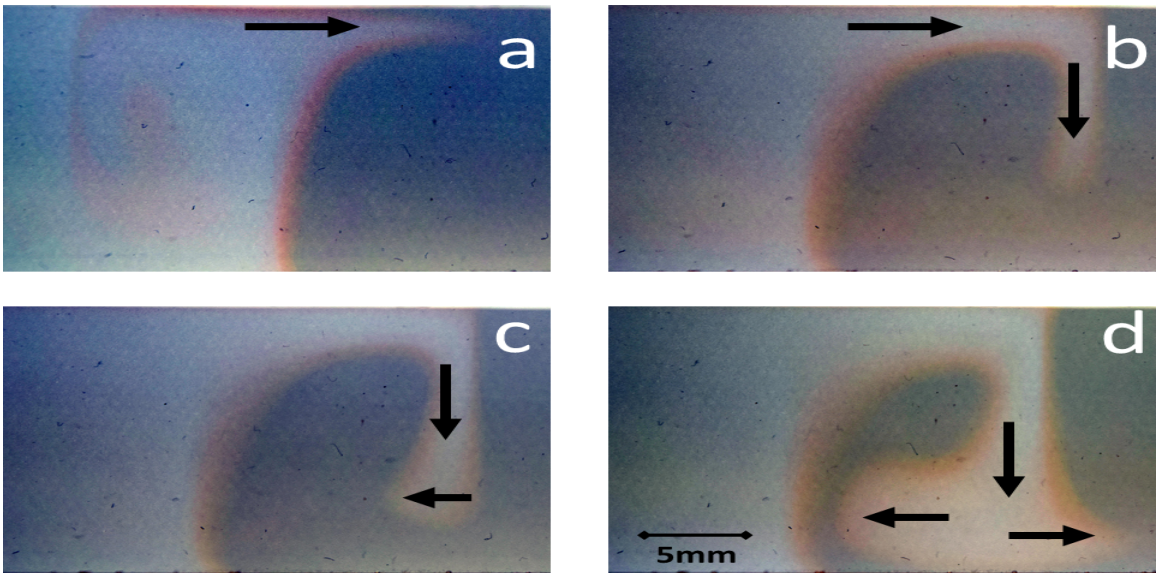

Figure 1.3: Experimental results showing the time evolution of a buoyancy driven instability. (a) t = 0min, (b) t = 2 min, (c) t = 3 min, (d) t = 5 min.

In the presence of gravity, density changes can cause buoyancy-driven instabilities, called double diffusive convection.[7] Consequently in an exothermic reaction

where chemical composition and temperature changes are present and there is a difference in diffusion coefficients, a buoyancy driven instability forms.

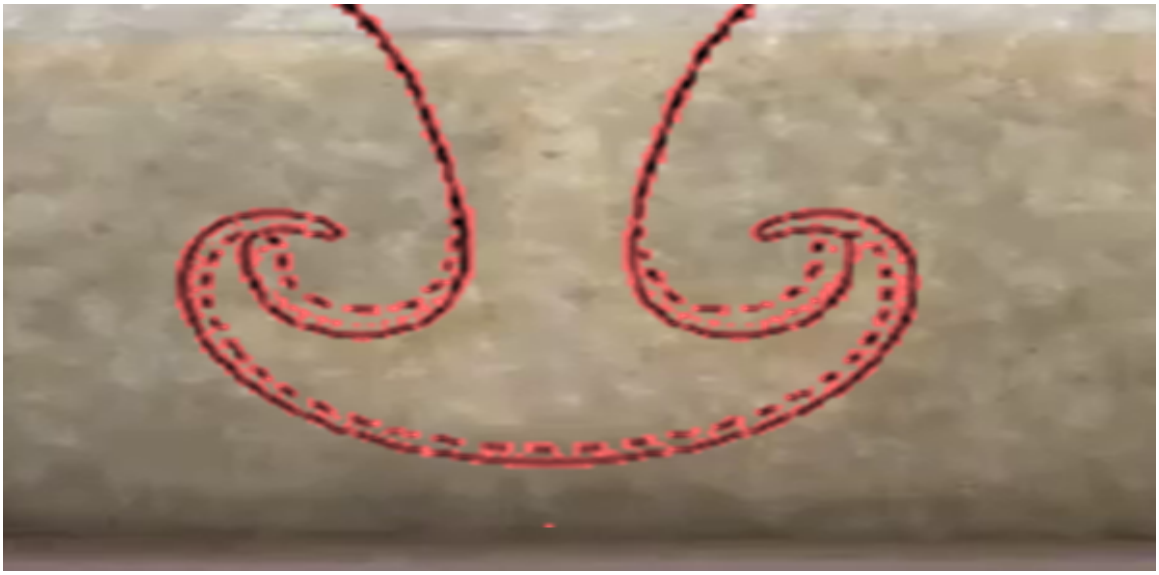

Figure 1.4: Rayleigh-Taylor Instability generated from the chlorite-thiourea reaction system. Overlay, a theoretical approximation of the Rayleigh-Taylor instability.

Buoyancy driven instabilities formed from double diffusive convection allow for Rayleigh-Taylor Instabilities to form at the interface between fluids of different densities. The extent to which fluids are mixed together by the instability is governed by properties of the individual fluids and usually characterized by the depth to which the lighter fluid penetrates into the heavier layer.[55] An example of a Rayleigh-Taylor Instability generated from the chlorite-thiourea system is depicted in Figure 1.4 with a simulated instability overlaid on experimental results.[56]

1.3 Flow Visualization

Flow visualization is an integral component of experimental fluid dynamics. The key aspect is that, compared to other tools, it allows for many properties of the flow field to be visualized.[57] Observing flow of fluids is not a new endeavor and can be

traced back to Reynolds and Prandtl's pioneering fluid dynamics work in the late 19^{th} century.

From the earliest work to the present day, flow visualization methods generally fall into one of three categories: 1) Adding foreign materials into a flow; 2) Optical flow visualization; 3) Flow field visualization by heat or energy input. The first category is the most applicable in our approach.

Adding foreign material into a flow can be as simple as adding dyes or additional particles into solution. In the case of a reacting flow, such as the chlorite-thiourea system outlined above, it is also possible to use pH indicators. Additionally, in his pioneering work, Prandtl used aluminum powder and ferrous mica to observe fluid flows around a stationary object using cinematography equipment.[18,19]

The traveling wave and reaction front in the chlorite-thiourea reaction is characterized by a sharp production of H^+. Thus, pH indicators can be used to follow the wave front. This procedure has been used extensively and is a well documented method to quantify and track traveling waves generated by autocatalytic reactions.[1,7,27,58,59]

Conventionally, a single indicator is used. Indicators include Congo red, methyl red, or bromophenol blue, at a concentration of one percent, roughly one to three millimolar.[1,7,32,50] At these concentrations indicators can act as buffers and, in the case of Congo red can inhibit isothermal surface tension changes.[1,7,60] To address these issues, a unique combination of two indicators was used; they were present at much lower concentrations than previously reported experiments and were coupled with MATLAB code to extract more detailed information from the reaction fronts.

For experiments conducted for this thesis indicator concentrations were $2.38x10^{-8}$M for bromophenol blue and $1.22x10^{-9}$M for methyl orange. Over this concentration range, indicators were present at five orders of magnitude lower con-

centration than published work on the chlorite-thiourea and chlorite-tetrathionate systems.[1,4,7,58,61,62] As previously reported, reducing the concentration of indicators minimized any effects on surface tension or activity as reaction buffers.[1,7]

Previous work on the chlorite-thiourea system displayed hydrodynamic behavior dominated by Marangoni convection.[27,50] This was evident by rapid propagation of chemical waves along the surface of the reaction vessel without associated thermal plumes and reaction-diffusion-convection behavior. Results in Chapter 2 show that reducing indicator concentration makes it possible to visualize the interplay between Marangoni convection, reaction diffusion, and thermally induced density changes. This combination of effects were not discernible in previous studies.[27,50]

The combination of indicators created a brown reactant solution. From bleaching effects, and the fact that both bromophenol blue and methyl orange turn light yellow in acidic conditions, the product solution was clear. The two to three millimeter thick reaction front, however, displayed a red orange color. Because of the low concentrations of indicators used, this color was very faint. These complications needed to be overcome to effectively observe the system behaviors.

1.3.1 MATLAB Image Enhancement

In order to make use of images recorded at low indicator concentrations, it was necessary to enhance their colors. This was done using MATLAB code, that separated each of the color channels from the RGB (Red, Green, Blue) image. Figure 1.5 shows a raw image, left, taken of the reaction system. Any detail in the raw image appeared to be washed out and provided insufficient information to analyze. The right image of Figure 1.5 shows the same image after undergoing enhancement. In this image the reaction front is clearly seen as a red-orange color. The unreacted bulk solution is blue corresponding to the bromophenol blue indicator and the reacted solution is

clear due to bleaching. A 2 mm grid was then overlaid on the image to visually aid in tracking wavefront movement.

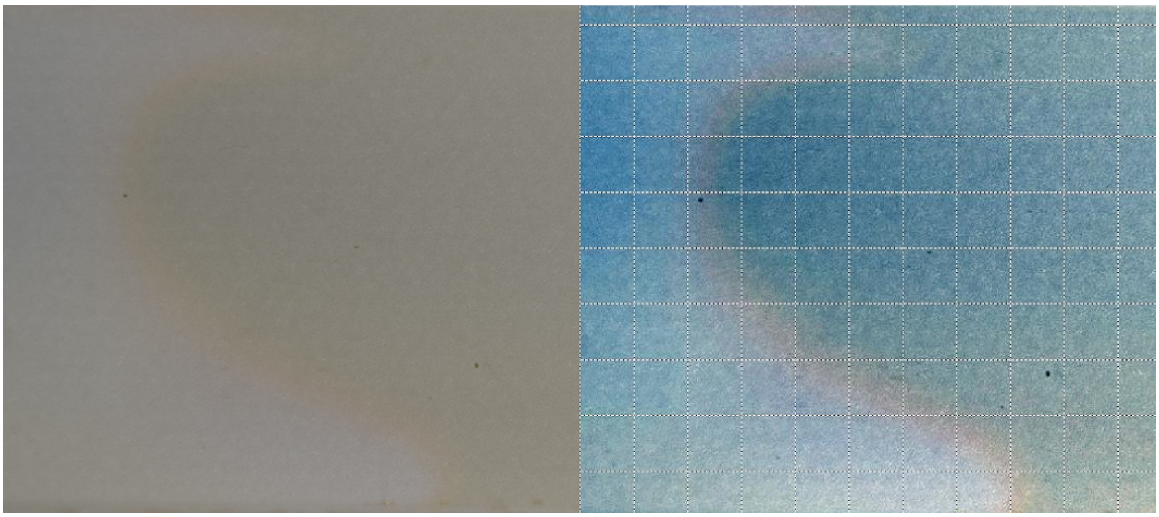

Figure 1.5: Demonstration of the two indicator system. Left: Reaction front in a raw image, nothing visible. Right: Same image after enhancement, with grid added.

In the raw image, the colors in each channel Red, Green, Blue (RGB) were bunched over a small pixel intensity range. This leads to a homogenous and indistinct image. The MATLAB code spread the pixel count, for each color channel, across the full spectrum of pixel intensities. Histograms showing this change are shown in Figure 1.6. The result of this change is that each color is visually distinct, while preserving the inherent background image.

The enhanced RGB images could be converted into a hue/saturation/value (HSV) image. HSV is used extensively in computer vision and vision analysis for feature detection.[63] With the converted HSV image it was possible to visualize the reaction front by the orange-red color. The orange-red color of the reaction front is isolated to produce a true black color on a grayscale spectrum. A demonstration of HSV conversion is shown in Figure 1.7 where the enhanced image from Figure 1.5 is on the left and the HSV converted image is on the right.

After converting an image to HSV the acid wave front can be quantified. There

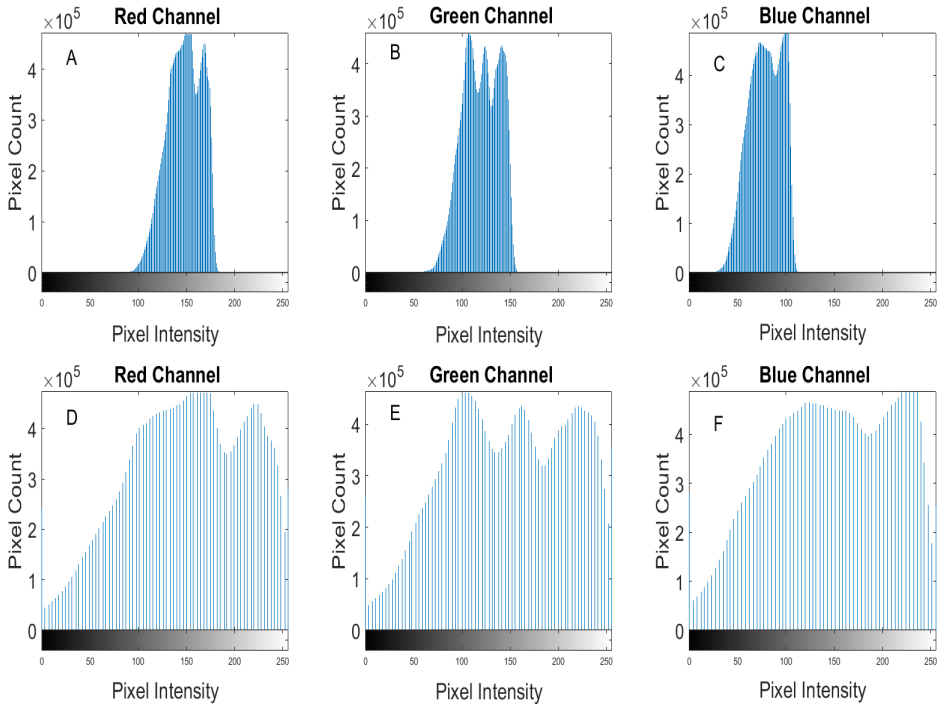

Figure 1.6: Histogram of the RGB color channels for the images in Figure 1.5. Subplots A, B, and C represent the RGB channels before enhancement. Subplots D, E, and F represent the RGB channels after enhancement.

is a one minute time difference between Figure 1.7a and 1.7b. In Figure 1.7a the thickest part of the wave is seen at the surface at 4.30 mm. This build up of products and heat causes Marangoni convection to drive the wave to the right. As the wave progressed, the wavefront becomes thinner and in Figure 1.7b the wavefront measures only 1.04 mm. In contrast, the wave at the bottom of the vessel in 1.7a averages only 1.74 mm but the lower wave velocity causes products to accumulate. In 1.7b the lower wave measured 2.57 mm.

The MATLAB code provided a platform for tracking and quantifying these traveling waves. The images themselves included a scale of known length that allows for the conversion of pixels to millimeters (mm). This provided a consistent scale regardless of whether it was formed from a 4000 x 3000 pixel image or a 1080p frame

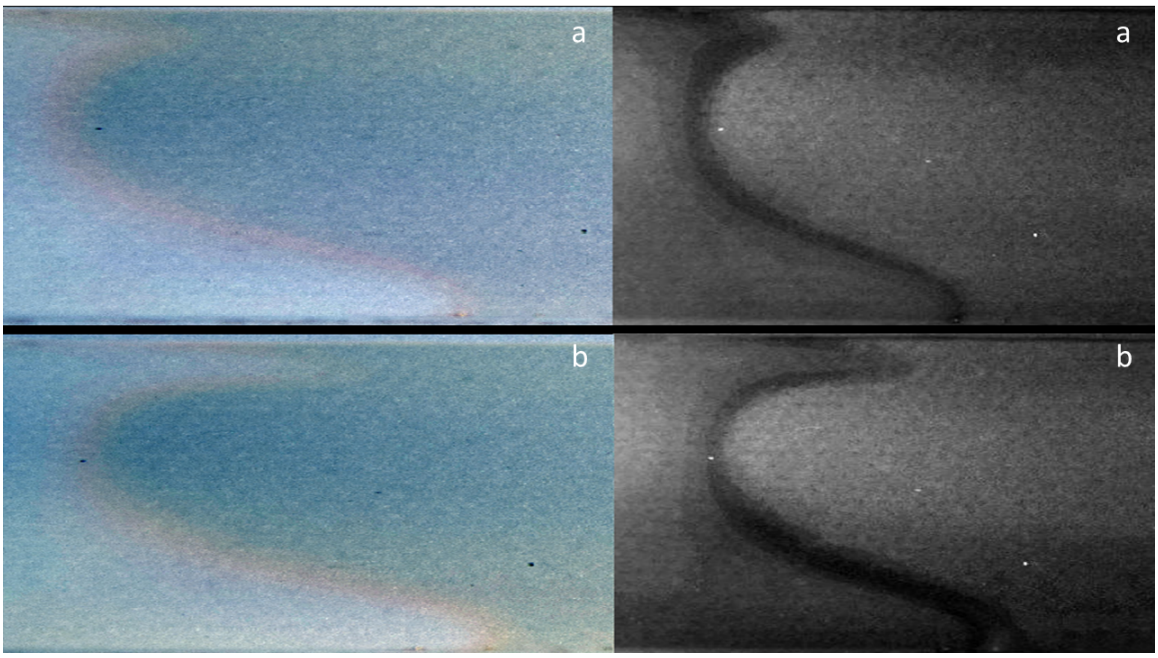

Figure 1.7: Demonstration of the two indicator system highlighting the reaction front. Left: Two images after MATLAB color enhancement. Right: Same images after color extraction to highlight the reaction front. (a) t = 0 min, (b) t = 1 min.

of a video. From direct measurement of the image it was possible to quantify thickness of the reaction front, direction and speed of growth, and direction and speed of wave propagation.

For accurate time measurements, video frames were recorded at a rate of 50 frames per second (fps) with a time accuracy of a hundredth of a second. Knowing the length, in pixels, and the time elapsed it was possible to track the velocity of wave propagation. For measurement of horizontal wave propagation, MATLAB code was used to extract the time stamp and frame data, and track the image, for a set amount of time or until no more motion was detected.

MATLAB code takes advantage of parallel computing, to enhance images and track reaction fronts. Parallel processing allowed each image or frame of video to be processed by a different core or thread of the central processing unit (CPU), greatly reducing time to compute and process results. The program is scalable on computers

ranging from two cores and two threads to eight cores and sixteen threads.

CHAPTER 2
VISUALIZATION AND TRACKING OF TRAVELING ACID WAVES GENERATED FROM THE CLORITE-THIOUREA REACTION

2.1 Introduction

In fluid dynamics, a wave can be considered any front of discontinuity that moves through a system.[23] Wave phenomena has been observed for many natural reaction-diffusion-convection processes.[64]

Traveling chemical waves appear to be due to the interplay between autocatalytic chemical reactions and diffusion.[65] In a reactive flow, waves transmit energy and mass over a distance. In the chlorite-thiourea reaction system three principle waves are present. These are chemical, thermal, and gravity waves.

The velocities of propagation and shapes of chemical waves are directly correlated to kinetics of reactions and diffusion rates.[66] Chemical waves contribute to both thermal and density waves. They cause thermal waves by acting as a source or sink of energy depending on whether the reaction is exothermic or endothermic, respectively. Depending on the densities of products produced, a reaction can also generate density waves.

For density wave propagation an acceleration field is required. Both chemical and thermal waves can provide an acceleration field suitable for creating density waves. Using the chlorite-thiourea system as an example, changes in chemical composition can lead to increased solution density, where products are more dense than reactants. However, increasing temperature leads to a decrease in solution density. A consequence of heat generated from the autocatalytic reaction causes an inversion

where higher density chemical products overlay on less dense reactants. This situation can lead to a vortex where misaligned density gradients grow exponentially in a nonlinear manner; which can lead to Rayleigh-Taylor Instabilities.

In the chlorite-thiourea reaction, the primary thermal wave is in the form of a convective wave. This thermal wave generated from the autocatalytic and exothermic reaction uses the temperature gradient created at the localized reaction front to drive density changes.[3,4] The density changes brought from exothermic fronts are usually negative, lowering the density at increased temperatures. The interplay between chemical, thermal, and gravity waves leads to several distinct behaviors. The time evolution of the flow is summarized in Figure 2.1. Note, thermocapillary flows require material balance and back flow of solution in the vessel.

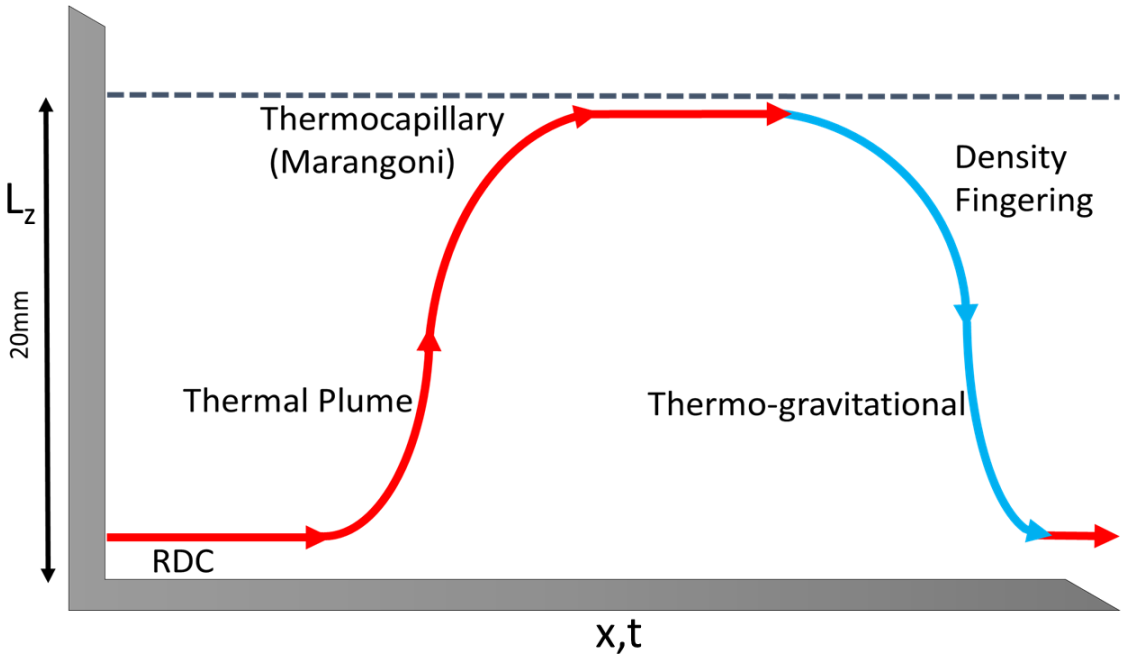

Figure 2.1: Schematic sketch of the time evolution of the flows observed in the chlorite-thiourea reaction system.

Autocatalytic reaction systems can generate localized pH gradients. These result in the appearance of a traveling acid wave into the unreacted bulk solution

that is spatially constrained by diffusion of the autocatalyst. While the work in this thesis used a chemical reaction to generate an acid front, the chemical reaction is ancillary to the result. In fact, the acid wave front could be generated by any number of methodologies, such as electrochemistry induced isoelectric, external effects, or solute gradients.[37,67,68]

A complication of autocatalytic chlorite-based reactions is that initiation of the reaction is stochastic.[69] In order to generate a traveling wave, reactions must be initiated by an external source.[1,3,4,61] In the absence of initiation, the stochastic nature of the reaction can cause initiation at multiple points in a reaction vessel. This is due to minor interfacial differences, such as the light source being too close to the reaction vessel causing localized heating that can trigger the reaction. An example of conflicting waves generated by stochastic initiation is shown in Figure 2.2.

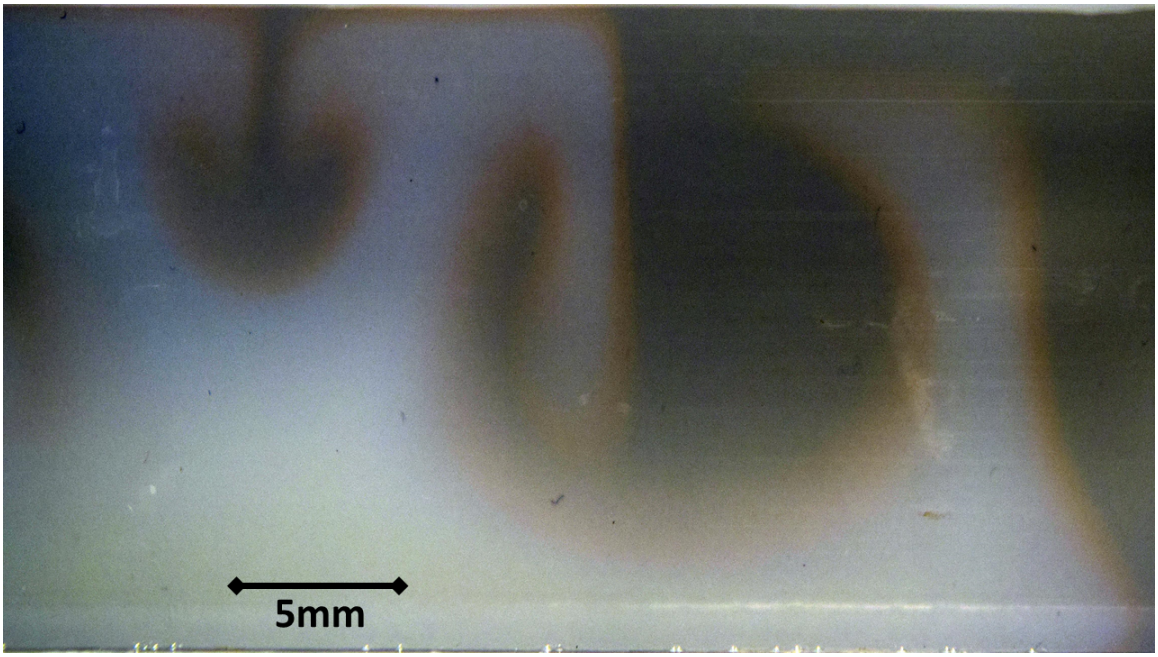

Figure 2.2: An example of competing waves generated by stochastic initiation. Chlorite concentration was 4.00 x 10^{-3} M while thiourea was much lower than standard conditions at 1.68 x 10^{-4} M.

The main product of the chemical reaction is a large change in pH resulting

in generation of an acid wave front. Observation and quantification of waves is primarily accomplished with the use of pH indicators. Section 1.3 describes how pH indicators can impact hydrodynamic behavior. To minimize effects of pH indicators on hydrodynamic motion, a novel approach was utilized to reduce the concentration of indicator by roughly five orders of magnitude compared to what has been reported in the literature, as described in Section 1.3. However, for comparison hydrodynamic results from previous chlorite-thiourea work was recreated using full indicator concentrations with results reproduced to match the original publication.[32] This experiment served as the baseline for the effect of pH indicators on hydrodynamic motion for the chlorite-thiourea system.

2.2 Experimental

2.2.1 Materials

The following analytical grade reagents were used without further purification thiourea (Aldrich); bromophenol blue and methyl orange (Fisher). Sodium chlorite is sold in in a technical grade ($\sim$ 80 %) and a single recrystallization (acetonitrile-methanol-water mixture) was used to purify to >98%. The analysis of sodium chlorite was performed iodometrically by adding excess acidified iodide and titrating against standard thiosulfate with freshly prepared starch as an indicator.[70] Stock solutions of sodium chlorite were prepared fresh for each set of experiments. All solutions were prepared in nanopure water. Sodium chlorite solutions were also stored in amber Winchester vessels wrapped in aluminum foil to reduce decomposition by light. The observation vessel used was a modified Hele-Shaw cell machined out of Plexiglas with dimensions measuring 260 mm long and a thickness of 10 mm . Total depth of the vessel was 30 mm, but reaction solutions were filled to not more than 20 mm in depth, leaving a 10 mm head. All recordings were made using a Nikon D3300 24.2 megapixel DSLR

camera.

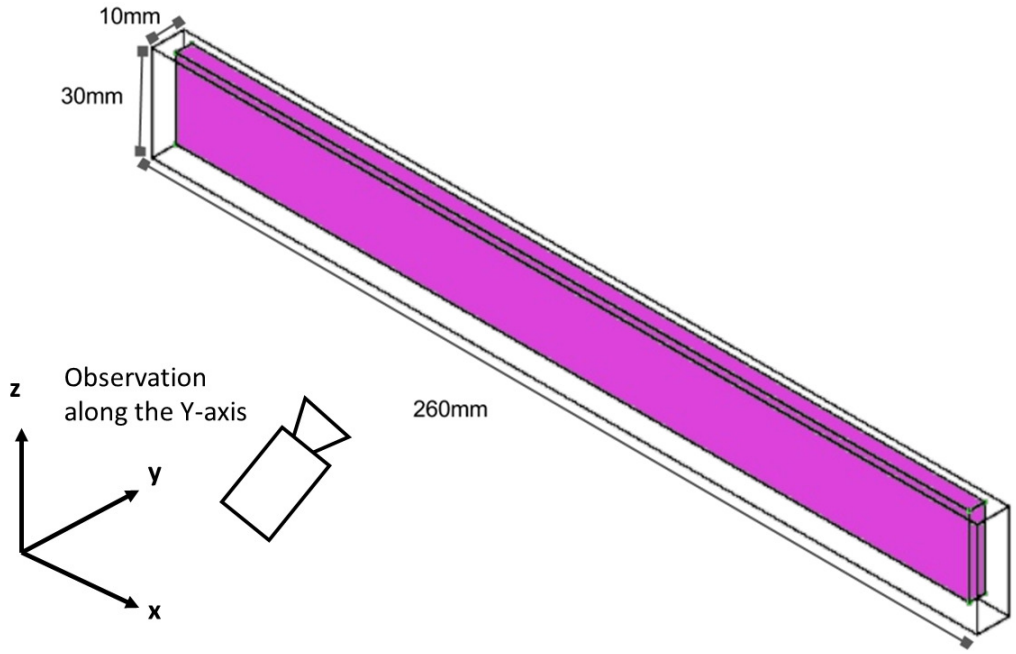

Figure 2.3: Modified Hele-Shaw cell. Exterior dimensions are shown. Reaction cavity dimensions (Length x Height x Depth) 250mm x 25mm x 5mm. Solution depth was 20 mm for all experiments. Waves were initiated electrochemically on the left side of the vessel.

2.2.2 Methods:

Chlorite, thiourea, and indicators were thoroughly mixed before being poured into the reaction vessel. After solutions were thoroughly mixed, they were allowed to settle until all physical ripples disappeared. They were triggered electrochemically with a a voltage of 3.0 V passed through a platinum electrode placed on one end of the vessel.

Reported experiments were run in excess of chlorite to ensure complete consumption of thiourea. Experiments performed at equal or excess amounts of thiourea were unreliable and exhibited random behavior.[71] Initial thiourea concentrations, $[CS(NH_2)_2]$ were fixed at 5.00 x 10^{-4} M and chlorite $[ClO_2^-]$ was varied from 2.00 x 10^{-3} to 1.00 x 10^{-2} M. Most experiments described in this chapter were performed

at 4.00 x 10^{-3} M chlorite, unless noted otherwise. For all experiments performed, pH indicator concentrations were fixed at $2.38x10^{-8}$ M for bromophenol blue and $1.22x10^{-9}$M for methyl orange.

Chlorite concentrations were the sole factor, at fixed thiourea concentration, for determining reaction rates, temperature generation, and pH change. Solution pH was determined before and after the reaction using a Fisherbrand Accumet pH meter. Temperature changes were measured using a rapid response temperature probe.

2.3 Results & Discussion

The geometry of the vessel was essential in determination of the type of waves that were produced. To distinguish between Marangoni, buoyancy, and density effects, a two-dimensional system was chosen. For the modified Hele-Shaw cell used for in this work, the narrow width allowed for pseudo two-dimensional behavior. The narrow gap width suppresses Rayleigh-Bérnard convection that would be expected in a wider vessel.[4,72,73] It was reported that Hele-Shaw cell gap widths under 10mm are sufficient to promote 2-D and suppress three dimensional behavior.[1,4,51,74]

Hydrodynamic behaviors associated with the chlorite-thiourea reaction exhibit the to ideal behavior in Figure 2.1. The time evolution of hydrodynamic behaviors are shown in Figure 2.4. Figure 2.4a shows idealized behavior corresponding to Figure 2.1. In 2.4b Marangoni convection along the surface of the vessel is arrested, presumably by interfacial defects causing density fingers to form.

Velocity of the descending finger in 2.4b was 7.92 mm min^{-1}. This velocity slowed as it neared the bottom of the vessel in 2.4c and back flow from Marangoni convection caused the wave to be pushed back towards the product solution. At the bottom of the vessel reaction-diffusion-convection (RDC) proceeded to push the wave forward at 2.38 mm min^{-1} for $\sim$5 mm before immediately transitioning into a thermal

plume between 2.4c and 2.4d. Because the plume opposed gravity, wave velocity was noticeably slower than the density finger at 2.24 mm min^{-1}. 2.4e shows the rapid transition from plume to the Marangoni convection back to density finger (snalogous to Figure 2.4b). Figures 2.4f & g show another iteration of density finger back to plume. These transitions continued, with comparable wave velocities and distances, along the entire (250mm) length of the Hele-Shaw cell in a periodic manner until the

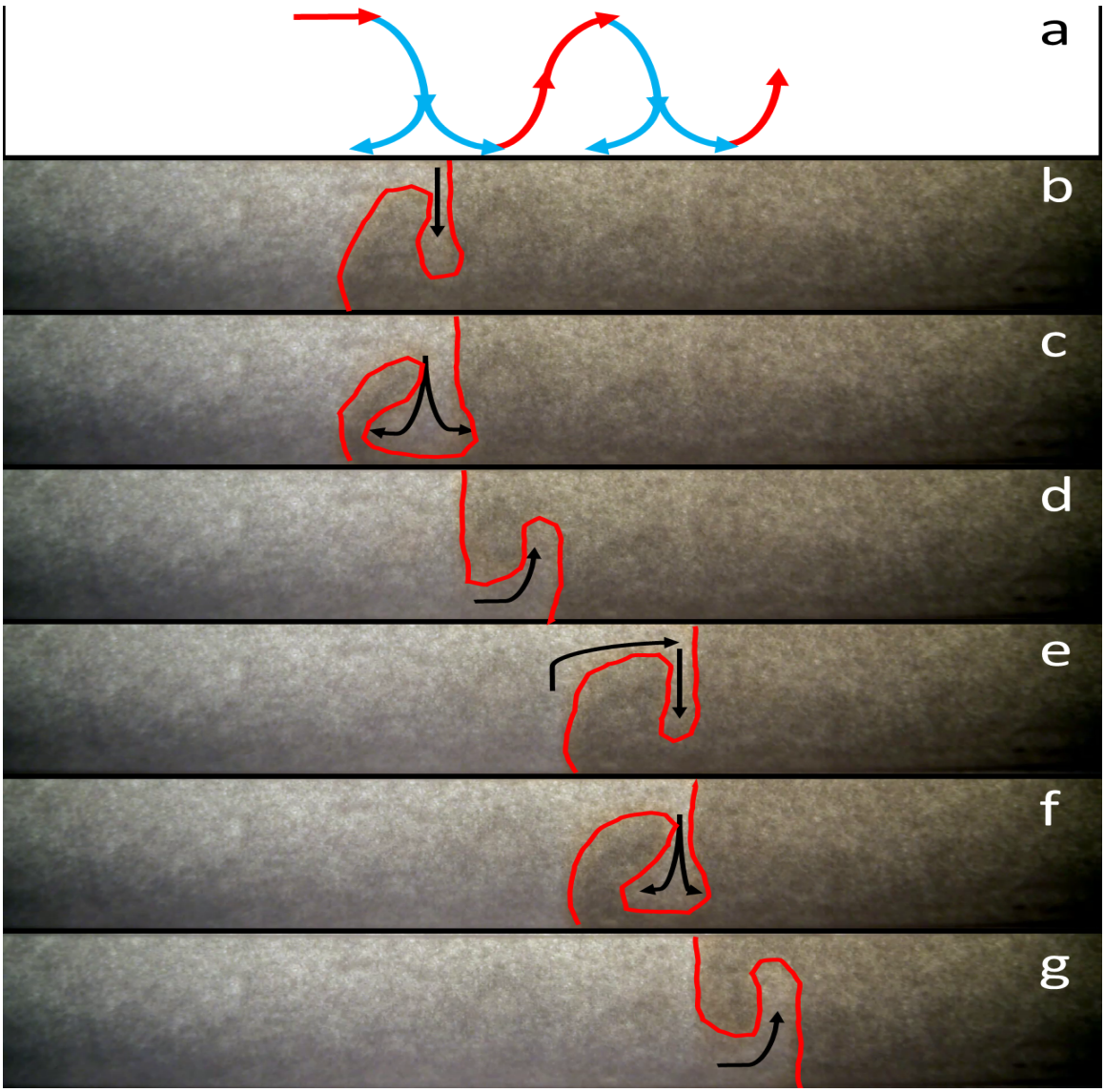

Figure 2.4: a – g: Time evolution of oscillatory finger and plume behavior. The reaction front is highlighted in red.

wave reached the closed boundary. This periodic behavior has not been previously reported with the chlorite-thiourea system.[32,50]

Performing the experiment, again using the same initial conditions, essentially the same behavior was observed but with different time dependence and flow distances. The differences, even under the same reaction conditions, shown in Figure 2.5 compared to Figure 2.4, revealed the stochastic nature of the reaction. The source of these differences was assumed to be due to mixing interactions between product and reactant solutions (the emergence of Rayleigh-Taylor instabilities). In another experimental run, Figure 2.5b shows that the RDC wave proceeded for roughly double the distance, ∼12 mm, compared to Figure 2.4.

Although RDC wave velocity, v_{RDC} was comparable at 2.52 mm min^{-1}. Interfacial effects are highlighted in 2.5b where the thermal plume bifurcated into three individual fingers. This minor perturbation was short lived as the rising wave expanded and consumed the individual fingers in 2.5c. Velocity of the ascending wave (v_{asc} in 2.5b and c was determined to be 2.06 mm min^{-1}.

Because of the extended distance the initial RDC wave covered, Marangoni effects are much more apparent. When the ascending wave reached the surface, Marangoni convection drove the wave back towards the product region of the solution and forward into the reactant region of the solution. Wave velocities, in both directions, were found to be comparable at 7.72 mm min^{-1} and -7.12 mm min^{-1}. Marangoni convection drove the wave in 2.5e ∼12 mm compared to 6 mm in Figure 2.4. Similar to the thermal plume, generation of a minor defect between the acid wave front and bulk solution causes the more dense products to overcome Marangoni convection and plummet into the less dense reactant solution zone. The density finger in 2.5e and f had a slightly slower descending velocity, v_{dsc}, of 6.85 mm min^{-1}. Once the wave reached the bottom of the vessel, in 2.4g, it bifurcated into separate RDC

waves and continued the observed periodic behavior until reaching the far boundary of the vessel.

Results of experiments showed that even under identical reaction conditions, individual wave velocities of hydrodynamic behaviors were not identical. However, by tracking wave velocities across multiple experiments, at the same initial reactant

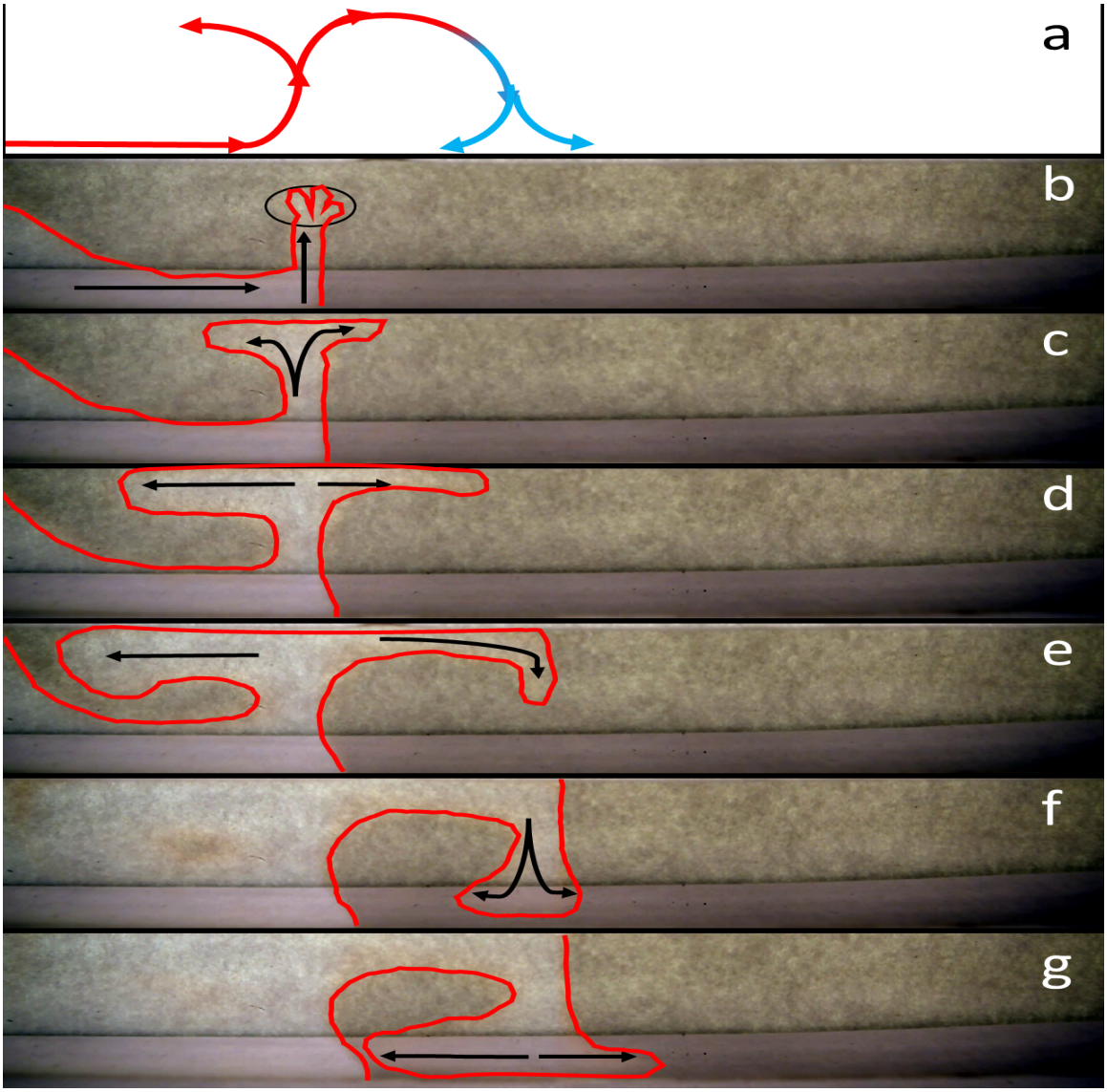

Figure 2.5: a – g: Example of stochastic thermal plume development and periodic behavior beginning from an reaction-diffusion-convection (RDC) wave. The reaction front is highlighted in red. Note (circled) in a, the interfacial defects bifurcating the plume.

concentrations, it was possible to determine the extent that velocities varied.

2.3.1 Wave Tracking

An example of wave quantification using pH indicators and MATLAB image enhancement is shown in Figure 2.6. Beginning with images that had already been color enhanced according to the procedure described in Section 1.3.1, it was possible to extract further details from the images. By conversion of enhanced images to HSV it was possible visualize details that are not naturally visible with the naked eye. In order to isolate the acid wavefront (red-orange color) in the color enhanced version the saturation channel of the HSV image was extracted and filtered. Isolation of the acid wave front is displayed as a greyscale image in Figure 2.6.

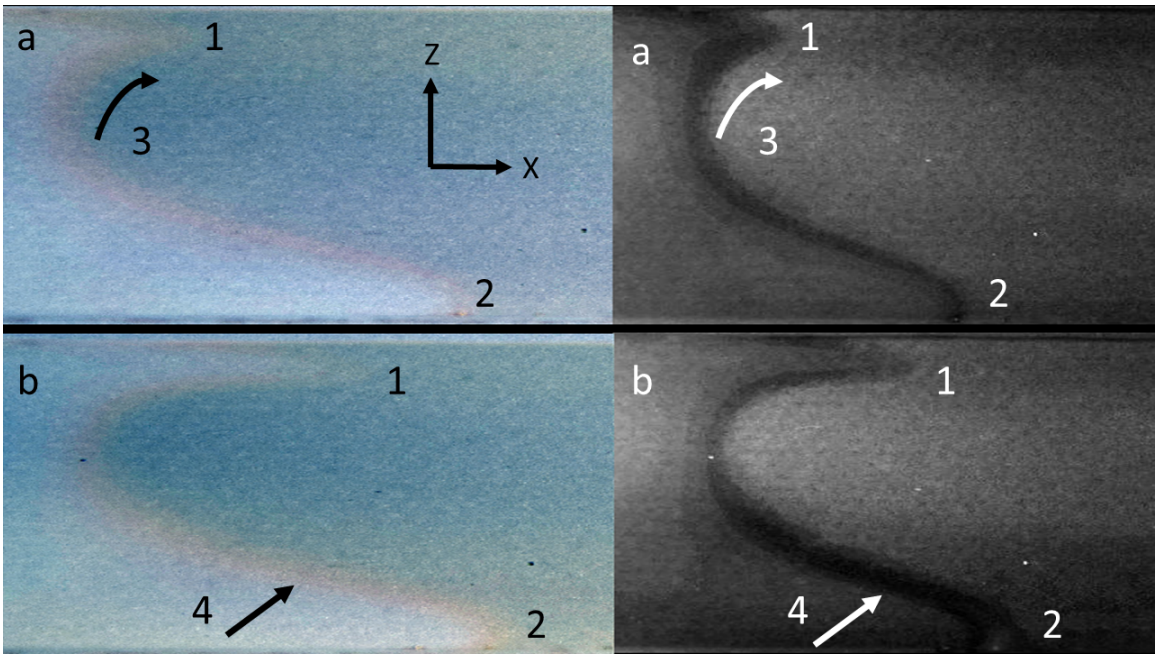

Figure 2.6: Color enhanced images converted to a HSV image for feature tracking. (a) t = 0 min, (b) t = 1 min.

In Figure 2.6a, the wavefront is thickest at the top of the wave at 4.30mm (1), thinnestat 0.90mm (2), with average thickness = 1.74mm. Between Figure 2.6a and

2.6b, wave (1) moves laterally at an average rate of 7.32mm min^{-1} and (2) moves at 2.71mm min^{-1}. During the transition from Figure 2.6a to 2.6b. the thickest part of the wavefront transitions from the surface to the bottom of the vessel, which can be attributed to lower forward velocity. It measures 2.57mm. The central portion of the wavefront shows no forward momentum and becomes the thinnest portion at 1.04mm as thermocapillary convection draws more of the reacting front to the top of the wave, seen in arrow (3), and reaction-diffusion-convection causes an accumulation along the bottom(4).

Further results of wave tracking are displayed in Figure 2.7. This data represents 50 experiments with between 8-10 periods of the fluid flow for each experiment at the standard reactant concentrations of 4.00 x 10^{-3} M chlorite and 5.00 x 10^{-4} M thiourea. $v_{Marangoni}$ represents the velocity along the surface of the reaction vessel with the z axis running vertically. v_{RDC} is the velocity at the bottom of the vessel. Similarly, $v_{ascending}$ and $v_{descending}$ represent the thermal plumes and density fingers, respectively.

Above results were for reactions run at a 20:1 ratio of chlorite to thiourea. At this ratio, average pH = 5.5 for reactant solutions. For product solutions pH fell between 2.7 and 3.2. Similarly, reactant solutions were kept and run at room temperature (298 K). The temperature increase associated with the reaction was found to be $\sim$2.8 degrees. Across the range of concentrations studied final pH varied between 1.5 and 3.5. Temperature changes were between 2.2 and 4.5 degrees. Note that pH and temperature values were determined by initial chlorite concentrations. Higher concentrations of chlorite corresponded to lower pH values and higher temperatures.

Previous work has shown that velocity determination for traveling acid waves in the absence of hydrodynamic motion can be approximated through utilization of a U-shaped glass tube 1cm in diameter.[2,66,75] The flat bottom of the "U" allows the

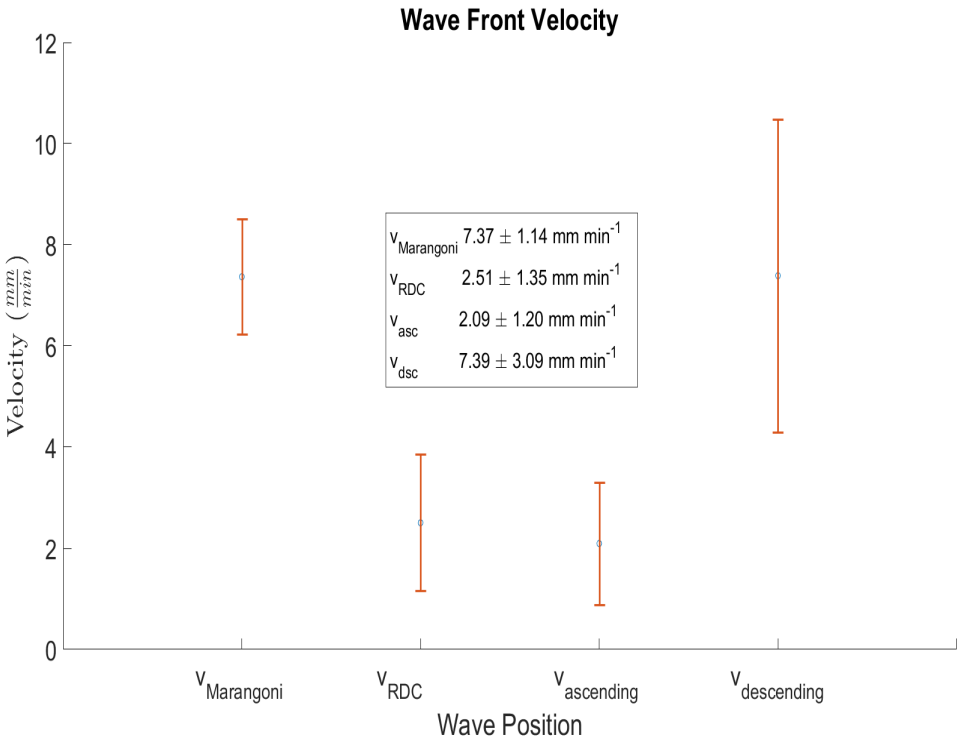

Figure 2.7: Measured wave speeds for Marangoni waves ($v_{Marangoni}$), RDC waves (v_{RDC}), thermal plumes ($v_{ascending}$), and density fingering ($v_{descending}$).

wave to travel horizontally with no surface or buoyancy effects acting as a pseudo one-dimensional system. For the primary reactant ratio of 20:1, the rate of wave propagation was found to be 1.4mm min^{-1}. Interestingly, across the concentration range examined there was an approximately linear response between initial chlorite concentration and wave velocity. Increasing chlorite concentration increased wave velocity

2.3.2 Chemical Model for Wave Front Propagation

Before creating a fluid dynamic model, it was essential to solve for the velocity flows of the simplified chemical model proposed in 1.2.4. Specifically, the reaction rate

constant for Reaction 1.12,

$$\dot{\omega_j} = k_f[\mathrm{ClO_2}^-][\mathrm{SC(NH_2)_2}]^1/2[\mathrm{H}^+]^2 \tag{2.1}$$

k_f was determined from 1-D modeling of chemical wave front propogation.[4,6,32,61] The 1-D model has the following form of the diffusion equation,

$$\frac{\partial[C_i]_{(x,t)}}{\partial t} = D_i \nabla_x + \sum_{j=1}^{n} \nu_{i,j}\dot{\omega_j} \tag{2.2}$$

Concentrations of species i at a specific time and location were determined by the diffusion equation according to Fick's Laws. Chemical kinetics were coupled to Fick's Laws with the rates, $\dot{\omega_j}$, and stoichiometries, $\nu_{i,j}$ for each chemical species. A three reaction model was assumed, and ionization of H^+ by OH^- was not factored into the model. Historically, calculations with this omission were shown to still generate accurate results.[2,59] The important chemical equations are:

$$\dot{\omega}_\mathrm{j} = \mathrm{k}_1[\mathrm{ClO_2}^-][\mathrm{SC(NH_2)_2}]^{1/2}[\mathrm{H}^+]^2 \tag{R 2.1}$$

$$\mathrm{H}^+ + \mathrm{ClO_2}^- \overset{k_{eq}}{\rightleftharpoons} \mathrm{HClO_2} \tag{R 2.2}$$

$$\mathrm{H}^+ + \mathrm{SO_4}^{2-} \overset{k_{eq}}{\rightleftharpoons} \mathrm{HSO_4}^- \tag{R 2.3}$$

Forward and reverse rate constants in Reactions R 2.2 and R 2.3 were from the literature values as summarized in Table 2.1.[6,27,50,59,61,76]

Likewise, diffusion constants for the chemical species were from the literature and summarized in Table 2.2.[77]

Integration of the 1-D model, Equation 2.2, was performed using MATLAB

Table 2.1: Literature rate constants for the one-dimensional model

Reaction	Forward Rate ($M^{-1}s^{-1}$)	Reverse Rate (s^{-1})
R 2.2	$1x10^{10}$	$1.38x10^{8}$
R 2.3	$1x10^{10}$	$5.75x10^{8}$

Table 2.2: Diffusion constants for chemical species

Chemical Species	Diffusion Constant (m^2s^{-1})
H^+	$1.4x10^{-8}$
$SC(NH_2)_2$	$7x10^{-10}$
ClO_2^-	$1.3x10^{-9}$
SO_4^{2-}	$1.1x10^{-9}$
$HClO_2$	$1.3x10^{-9}$
HSO_4^-	$1.1x10^{-9}$

2018a with the built-in partial differential equation solver. The model was arranged in a 1-D mesh 2 cm long with no-flux boundary conditions. The mesh was separated into 200 or 400 equally sized cells (there was no difference in results between sizes). This arrangement was consistent with similar models created for other autocatalytic systems.[5] Integration time steps were set to 0.1 s.

Initial concentrations for species in the bulk solution were set to those of the unreacted solution. To simulate electrochemical initiation of the reaction, for the first 10-20 cells of the mesh concentrations of chemical species were set to those of the product solutions at a pH = 3. The rate constant, k_f, for R 2.1 was initially set to $1x10^5$ $M^{-2.5}s^{-1}$ as determined for the chlorite–trithionite reaction system.[1] Rate constant values were varied over the range of $1x10^5$ to $5x10^6$ $M^{-2.5}s^{-1}$ by increasing the rate constant by $1x10^5$ per run. The distance the H^+ traveled at two minutes of reaction time was used to calculate the wave velocity.

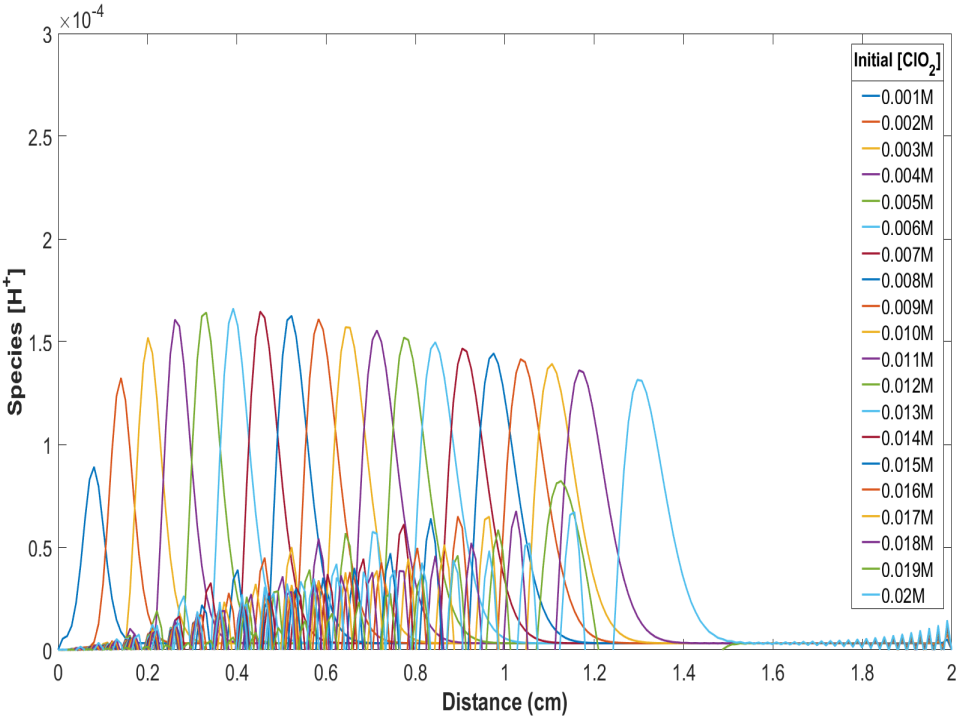

Figure 2.8: H^+ Wave front location at t = 2 min at a rate constant of $3x10^5$ $M^{-2.5}s^{-1}$. Inset: initial chlorite concentrations. Increasing chlorite concentrations resulted in an linear increase in wave front velocity.

The rate constant, $k_f$in Equation 2.1, was determined to be 3 $x10^5$ $M^{-2.5}s^{-1}$. k_f was evaluated by matching the modeled wave front velocity of H^+ with that measured for the 1-D system (1.4 mm min^{-1}). It turns out that, reaction rates were less critical than reactant concentrations. Formation of traveling acid wave fronts are a predominantly diffusion driven process. Reaction rates contribute little to overall wave velocity.[4,6] The minor waves of lower intensity, also shown in Figure 2.8, correspond to smaller proton wavefronts produced by minor equilibrium reactions to form hydrogen sulfate and chlorous acid (R 2.2 and R 2.3).

For all calculations, thiourea remained fixed while the concentration of sodium chlorite was varied to adjust the velocity of the H^+ wave. The H^+ wave speed as a function of $[ClO_2^-]$ is displayed in Figure 2.8. Calculated H^+ waves were found to

be ∼2 mm wide, consistent with the measured wave thickness. The rate constant for Reaction 2.1 was required for construction of the 2-D numerical simulation.

2.3.3 2-D Numerical Simulation for Wave Front Propagation

The 1-D model only accounts for chemical reactions and diffusive effects. Unlike the 1-D model, the 3-D model also accounts for advective and convective forces. Thermal and mass transfer are tied directly to the chemical reaction.

To simplify the simulation, a snapshot of the reaction vessel was used. Dimensions for the reference frame for simulation were 3 cm long by 2 cm tall. This reference frame provided a view consistent with experimental results. An adaptive, triangular mesh consisting of 77,448 elements was used to populate the reaction system. A feature of these adaptive meshes is that their individual sizes may vary and can thus provide more detail near boundaries. An example of the simulation geometry and mesh is shown in Figure 2.9.

All simulations were carried out in COMSOL Multiphysics 5.3a with the modules for Transport of Diluted Species in Porous Media, Laminar Flow, and Heat Transport in Fluids. Integration was performed by the standard back differentiation algorithm and direct PARDISO solver.[23,42,78,79] Absolute tolerance for simulations was left at the default value of $1x10^{-6}$. Simulations, were carried out under two conditions. First, the system was assumed incompressible with the applied Boussinesq approximation. This treatment is standard for modeling these type of autocatalytic systems.[1,3,4,6,7,28,30,53,62] Second, the system was treated as weakly compressible in which density changes induced by chemical reactivity were accounted for as part of the fluid flow.

Boundary conditions were the no slip, no flux, and Marangoni boundary. The left, right, and bottom of the reference frame in Figure 2.9 are an impermeable barrier,

therefore no slip and no flux. The top of the system uses the Marangoni boundary condition to represent a surface exposed to the atmosphere. Recall, the experimental reaction vessel was 25mm tall with the reaction solution only reaching to 20mm and exposed to the atmosphere. Similar to experimental conditions, all boundaries and the reaction solution itself were set to ambient temperature of 298 K.

Chemical species, initial concentrations, and reactions were maintained identical to those used experimentally in the 1-D system (section 2.3.2). Physical parameters for the chlorite-thiourea system were taken from the literature. Marangoni condition, Ma_T, $\sigma = -8.6x10^{-5}$ N m^{-1} K^{-1}; thermal expansion coefficient, β = -0.4 kg m^{-3} K^{-1}; isothermal density change, $\Delta\rho = 2.8$ kg m^{-3}.[33] As a dilute solution, the bulk properties were set to those of water at 298 K; fluid density, $\rho = 1000$ kg m^{-3}; thermal conductivity, $\lambda = 0.6$ J s^{-1} m^{-1} K^{-1}; and heat capacity, C$_P$ = 4180 J kg^{-1} K^{-1} at 298 K.[80]

Equations for this system were input directly into COMSOL for simulated solutions. COMSOL enabled a simple switch for applying the Boussinesq approximation of an incompressible fluid, or a weakly compressible fluid according to the full continuity equation of mass conservation in Equation 1.6.

Similar to the 1-D experiment, the reaction was initiated by setting initial concentrations of chemical species to those of the product solution, for the first 1 mm of the reaction vessel, to mimic electrochemical initiation. Experimentally following reaction initiation, the system would require 20-50 mm, of the 250 mm vessel before displaying periodic thermal pluming and density fingering. Unfortunately with the snapshot simulation that was used, the initial simulation proved to have insufficient length for these behaviors to manifest.

To rectify this issue, new initial conditions were introduced where instead of initiating along the entire boundary a lower portion measuring 6mm by 2mm was used

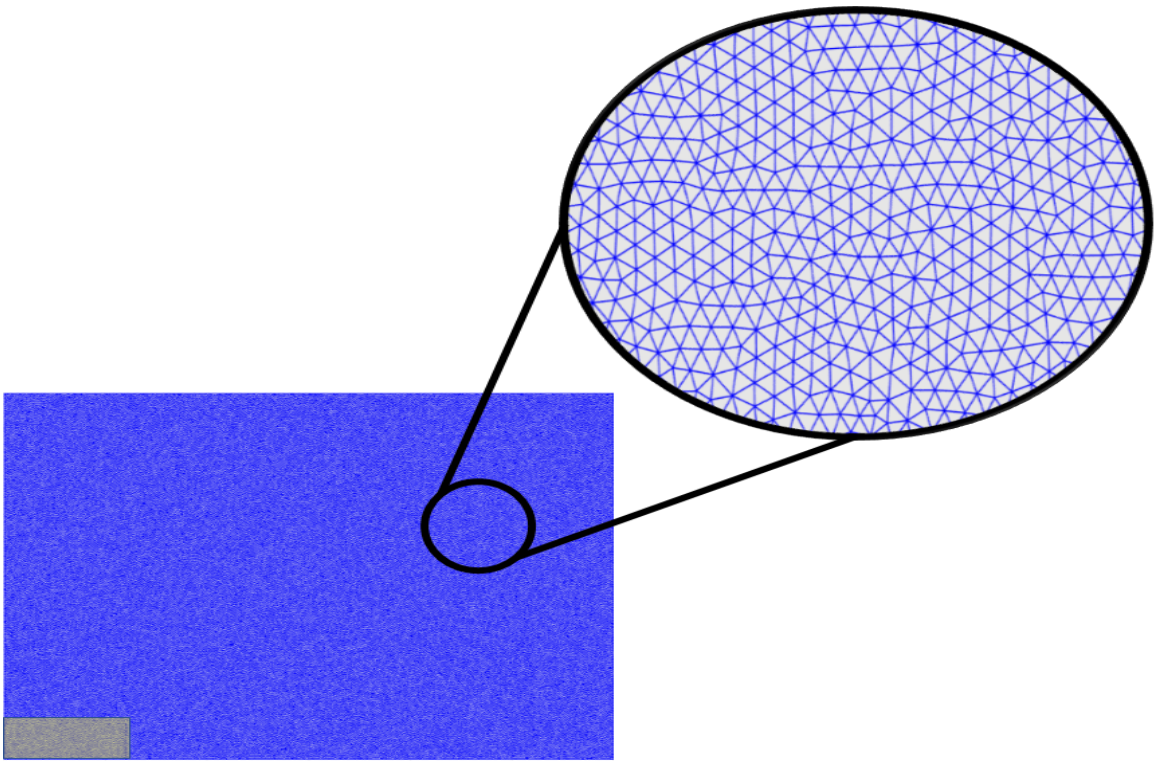

Figure 2.9: Simulation dimensions with a 77,448 triangular mesh. Adapted initiating conditions are highlighted in yellow. Inset: zoomed in view of triangular mesh. Each triangle represents an individual control volume.

to initiate the system, shown as yellow in the lower left corner of Figure2.9. Note that the initialization region was set to an initial temperature of 301 K, consistent with measured temperature change = 2.8 degrees. With this modified initial condition it was possible to simulate both the thermal plume and density fingering within the confines of the limited simulated system.

Figure 2.10 shows a comparison of experimental results (a-c) with simulated results (d-f). Simulations showed the exact same velocity and concentration profiles for incompressible and compressible fluids. In simulated examples, blue is the bulk unreacted solution while red corresponds to $[H^+]$ at pH 3.0. In Figure2.10a & d initiation of the reaction begins with formation of a thermal plume. The transition in Figure2.10b & e shows the Marangoni Effect pushing the wave front horizontally

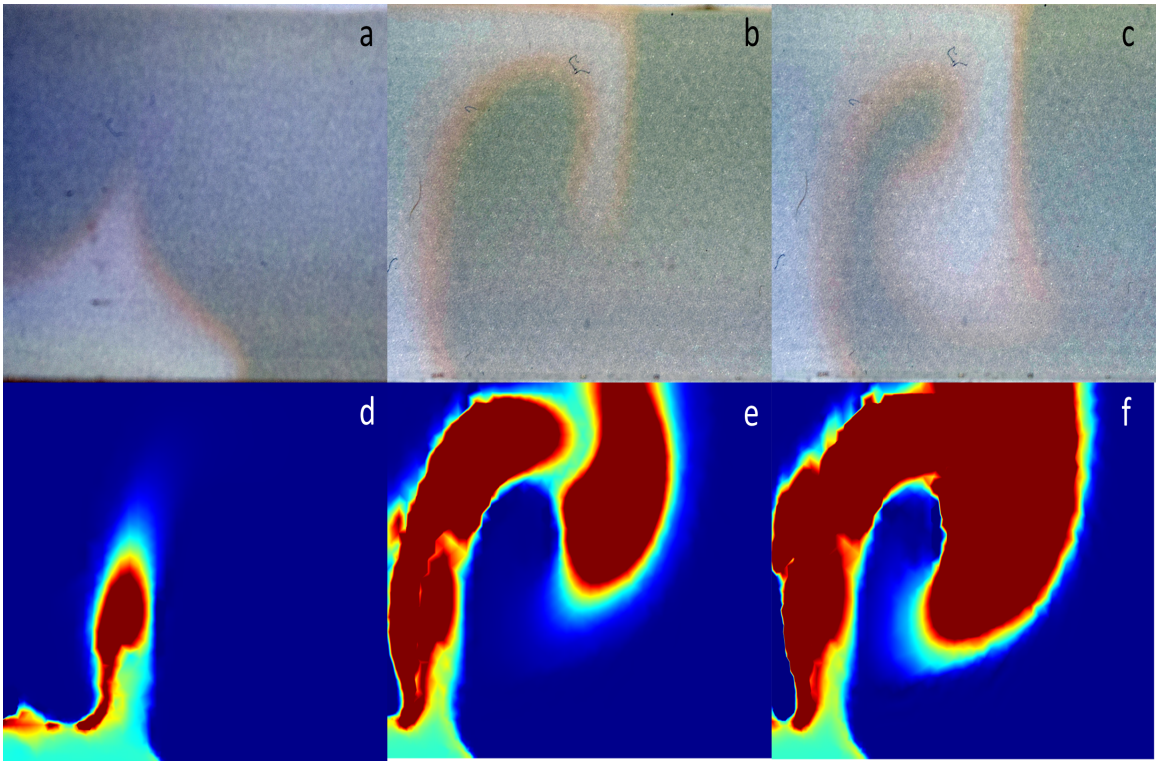

Figure 2.10: Comparison of experimental results to simulation.

before the increased density of the product solution causes density based fingering to occur. Figure2.10c & f display the backwards flow at lower z values due to Marangoni convection causing a circular current to form. As the fluid at the surface flows to the right there must necessarily be flow backwards to maintain material balance.

By tracking the velocity of the $[H^+]$ wave in simulations, it was possible to directly make comparisons with the experimentally measured fluid dynamics. A comparison of measured and simulated velocities for the $[H^+]$ wave are shown in Table 2.3.

Results in Table 2.3 show good agreement between experimental and simulated wave velocities. The stochastic nature of wave behaviors in experiments necessitated averaging across a large number of experiments (n = 50). The largest deviations of simulated to experimental results was observed for the descending and

Table 2.3: Experimental versus Simulated [H^+] wave velocity

[H^+] wave location	Experimental wave velocity (mm min^{-1})	Simulated wave velocity (mm min^{-1})
$v_{ascending}$	2.09 ± 1.20	1.83
$v_{descending}$	7.39 ± 3.09	6.07
$v_{Marangoni}$	7.37 ± 1.14	8.39
v_{RDC}	2.51 ± 1.35	2.35

Marangoni waves. For the descending wave, the limited geometry of the simulation may have caused the density finger to experience interference from back-flow caused by Marangoni convection. The Marangoni convection velocity may be impacted by literature values of the Marangoni condition measured for the chlorite-thiourea system. However, in all cases, simulated results fell within the standard error of the experimental results.

2.3.4 Summary

Previous experiments conducted on the chlorite-thiourea system, at conventional pH indicator concentrations only displayed Marangoni convection with density fingering.[27,32,33,50,76] Results in this chapter demonstrate that with substantially lower concentrations of indicator, and corresponding reduction in the surface tension gradient, alternating density fingering and thermal plume formation could be seen.

Simulated [H^+] wave velocities were comparable to the average values from experiments and were within the margin of error for measured results. Simulated wave velocities and dynamical behaviors provided support for our model and validity of governing equations and parameters that were employed.

With a linear response between chlorite concentration and velocity rate dependence of the reaction on chlorite is approximately first order; thus greatly simplifying

the problem. Since observed hydrodynamics are governed by chlorite, a full accounting of the complicated chemical kinetics of the chlorite-thiourea reaction was not necessary to investigate hydrodynamic behavior generated from the chlorite-thiourea system.

The stochastic nature (Figures 2.4 & 2.5) highlights the difficulty of using autocatalytic reaction systems to generate hydrodynamic motions. Both the chlorite-thiourea and chlorite-tetrathionate reactions are extremely complicated with 13 individual reactions, autocatalysis, supercatalysis, and autoinhibition.[2,6,25,26] Even so, experimental hydrodynamic results (for both systems) clearly show that detailed knowledge of the underlying chemical kinetics is mostly irrelevant, with little measurable effect on hydrodynamic behavior.

Over the time scale of the simulation, results of the compressible and incompressible models were indistinguishable, with identical $[H^+]$ wave and flow velocities. This begs the question on the importance of treating the system as compressible. One result, that has nothing to do with the physical system, is computational time. When running the system as incompressible, the average computational time for convergence of the model was 229 seconds; when running as compressible the simulation was completed in 184 seconds. The net result, a 20% time savings.

For the snapshot simulation used, there was no difference in results and time savings were modest. It might be that the system was too limited for these differences to manifest. However, if simulations were expanded to the full 250mm reaction vessel (or larger systems) and a third dimension was introduced, measurable differences between treating the fluid as compressible versus incompressible might be observed. Likewise, for larger systems and longer simulations, time savings could be amplified by treating the system as compressible. In the future, time savings from treating the system as compressible can be quantified by doubling the dimensions of the model

geometry to verify the time savings remain at 20% or scale based on the size of the model. At a minimum, these results show that there is no computational savings for treating the system as incompressible.

A question arises as to why the "simpler" model required more processing time. The Boussinesq Approximation is only valid when nonlinearities in the system are small. Since more time was required to solve for the incompressible system, it suggests that the approximation may be sub-optimal or invalid.[10] While the validity of Boussinesq Approximation has been proven for these types of chemical systems, time savings most likely reside with the nature of numerical solvers used in modeling software.

Solving the full Navier-Stokes equations allowed the solver to avoid errors that result from rounding during the approximation.[10] Also, any time savings resulting from approximations likely cancelled by having to recompute those values for the other time dependant parameters of the system, such as momentum. Our results show that a full application of Navier-Stokes equations should be standard for simulating reactive flows whether generated from autocatalytic reactions or any other method.

CHAPTER 3
CONCLUSION

3.1 Overview

The field of studying the fluid dynamic behavior of autocatalytic reaction systems is relatively small and somewhat fractured according to the specific reaction of interest of their parent laboratory, whether chlorite-tetrathionate or chlorite-trithionate. Those systems display extremely complex chemical kinetics with supercatalytic activity.[6,77] The relatively simpler with regards to chemical kinetics, chlorite-thiourea system, has been neglected for a number of years prior to undertaking this project. Along with the lack of established models this made the chlorite-thiourea system perfect to challenge assumptions and approximations used in the more complex systems.

In these systems, the propagating $[H^+]$ wave front is necessarily visualized with pH indicators to show the change in pH as the reaction progresses. However, the nature of chlorite is that it acts as a bleaching agent that has the effect of washing out the color of the indicator over time.[81] This has caused researchers to use high concentrations of pH indicators to enable visualization of the autocatalytic wave fronts. A negative consequence of this heavy use of indicators is that the indicators themselves act as a buffer, absorbing H^+ thereby changing the reaction dynamics and acting to change surface tension of the bulk solution.[7] As detailed in Chapter 1, indicators used in these experiments were *five orders of magnitude lower* in concentration than comparable experiments.[1,4,7,58,61,62]

Low concentrations of indicator allowed for detection of behaviors in the chlorite-thiourea system (Chapter 2) that have never been detected in previous studies of the

chlorite-thiourea system.[27,32,33,50,76] In Chapter 2 it was shown that the system displayed an oscillating pattern of thermal plumes and density based fingering, among other more complex motions. However, minimal concentration of indicator made the wave fronts increasingly difficult to distinguish and analyze. This problem was overcome in a two ways. First, MATLAB code was written to enhance the color spectrum of the videos and images allowing for more effective visualization by eye, detailed in Section 1.3. Second, a combination of two indicators was used, bromophenol blue and methyl orange. This combination, while still bleached and essentially clear in the product solution, was able to highlight the reaction front as an orange color allowing for detailed analysis of the H^+ wave front itself; in addition to the bulk chemo-hydrodynamics.

Novel results generated from these experiments confirm that pH indicators play a prominent role in manipulating hydrodynamic motion of these systems. By greatly reducing the concentration of indicator, it is possible to visualize a more accurate representation of the chemo-hydrodynamic system. Also, we are unaware, of any published experimental results showing direct visualization of the H^+ wave front, other than theoretically. It is encouraging that the visualized wave front measured $\sim$2mm on average and was consistent with theoretical determinations of $\sim$1.6mm for the chlorite-tetrathionate system.[5]

Without the benefit of previous chemo-hydrodynamic models to build off of, a first principles approach was taken based on work done on the chlorite-tetrathionate system. This approach required a simplified chemical model tailored for the chlorite-thiourea system. Rate constants were calculated using self-written code in MATLAB for a one-dimensional system to determine reaction wave velocity as a function of rate constant. This rate constant was a major requirement for subsequent generation of 2-D numerical simulations.

The relatively simpler chemical kinetics of the chlorite-thiourea system in combination with experimental results that minimized collateral effects of indicators provided a strong basis for generating a numerical simulation. There is an extensive body of work done on simulating the chlorite-tetrathionate and chlorite-trithionate systems; and they all universally rely on the Boussinesq Approximation, that treats these systems as incompressible.[1,4,6,30,39] However, a key factor of these reactions is the conversion of lighter reactants into heavier products. In a fixed volume cell conventionally modeled with adaptive mesh grids, results implied that in a finite volume the fluid is compressible. In an effort validate the accuracy of treating the fluid system as incompressible, in Section 1.2.8 a model was developed that instead treated the system as compressible. Results were then compared, under the same conditions, using the simplifying Boussinesq Approximation.

A snapshot numerical simulation of chlorite-thiourea system was created to test the applicability of the Boussinesq Approximation and effects of inherent assumptions. Details of the model were presented in Section 2.3.3. Simulated chemo-hydrodynamic behavior of the model was in good agreement with experimental measurements. It was determined, that use of simplifying assumptions compared to solving the full Navier-Stokes equations proved indistinguishable and agreed with experimental results. However, computation time increased 20% compared to solving the full set of equations.

Differences between solving methods may eventually become more pronounced in a larger and/or more complex model where the small differences in compressibility can manifest over time. At a minimum, results demonstrated that a compressible model is not any more resource intensive to solve compared to use of a non-compressibility approximation. Therefore future numerical simulations of autocatalytic chemical systems should apply a full compressible model. In the future,

compressible models may prove more broadly applicable to systems that do not rely on autocatalytic behavior, as demonstrated in cases for CO_2 dissolution.[29,60,82]

3.2 Future Directions

A field that presents an exciting opportunity for applying these chemo-hydrodynamic models is in the field of macromolecular chemotaxis. Macromolecular chemotaxis concerns how a macromolecule; large molecules such as proteins, nanoparticles, or polymers; reacts to a gradient or driving force.[67] Driving forces may consist of solute, electrochemical, or energy gradients. This contrasts with conventional chemotaxis which concerns itself motion of an organism driven by chemical stimulus.[83]

In an effort to link chemo-hydrodynamics to protein biophysics, a simple model was constructed for an electrochemical device to separate four major plasma proteins in a microfluidic device based on their isoelectric points and an induced gradient, utilizing the same equations as used in Section 2.3.3. It was possible to determine partitioning of proteins into each outflow channel as shown in Figure 3.1, which could lead to a microscale method for protein separation by electrochemical means.

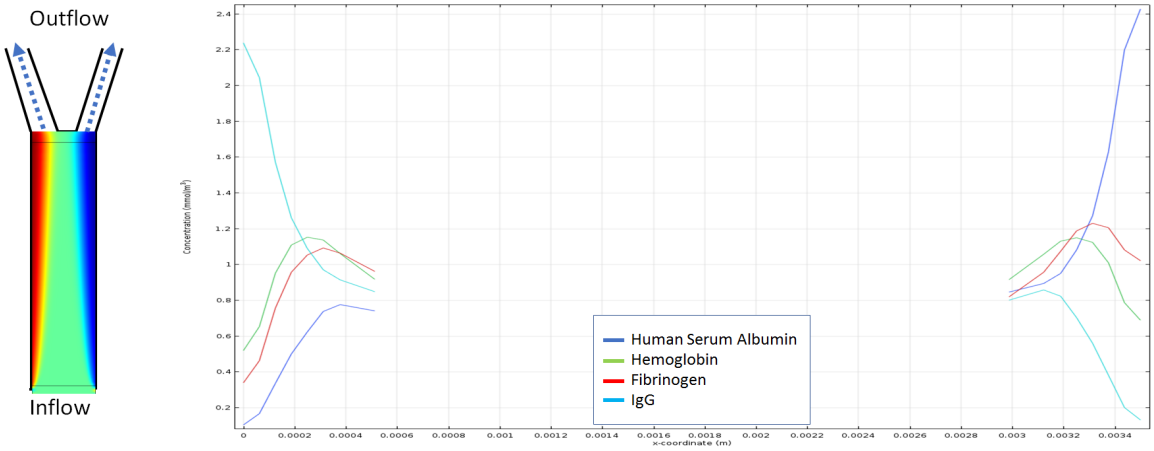

Figure 3.1: Electrochemical gradients to separate proteins in blood plasma.

REFERENCES

[1]Y. Liu, W. Zhou, T. Zheng, Y. Zhao, Q. Gao, C. Pan, and A. K. Horváth, "Convection-induced fingering fronts in the chlorite–trithionate reaction", The Journal of Physical Chemistry A **120**, PMID: 27059304, 2514–2520 (2016).

[2]Á. Tóth, D. Horváth, and A. Siska, "Velocity of propagation in reaction–diffusion fronts ofthe chlorite–tetrathionate reaction", Journal of the Chemical Society, Faraday Transactions **93**, 73–76 (1997).

[3]T. Tóth, D. Horváth, and Á. Tóth, "Thermal effects in the density fingering of the chlorite–tetrathionate reaction", Chemical physics letters **442**, 289–292 (2007).

[4]G. Schuszter, G. Pótári, D. Horváth, and Tóth, "Three-dimensional convection-driven fronts of the exothermic chlorite-tetrathionate reaction", Chaos **25**, 064501, `http://dx.doi.org/10.1063/1.4921172` (2015).

[5]G. Peintler, G. Csekő, A. Petz, and A. K. Horváth, "An improved chemical model for the quantitative description of the front propagation in the tetrathionate–chlorite reaction", Physical Chemistry Chemical Physics **12**, 2356–2364 (2010).

[6]A. K. Horváth, I. Nagypál, and I. R. Epstein, "Three autocatalysts and self-inhibition in a single reaction: a detailed mechanism of the chloritetetrathionate reaction", Inorganic Chemistry **45**, PMID: 17112285, 9877–9883 (2006).

[7]C. Almarcha, P. M. J. Trevelyan, L. A. Riolfo, A. Zalts, C. El Hasi, A. D'Onofrio, and A. De Wit, "Active role of a color indicator in buoyancy-driven instabilities of chemical fronts", The Journal of Physical Chemistry Letters **1**, 752–757 (2010).

[8]D. D. Gray and A. Giorgini, "The validity of the Boussinesq approximation for liquids and gases", International Journal of Heat and Mass Transfer **19**, 545–551 (1976).

[9]U. Bückle and M. Perić, "Numerical simulation of buoyant and thermocapillary convection in a square cavity", Numerical Heat Transfer, Part A: Applications **21**, 121–141 (1992).

[10]F. Schlegel, *Using the Boussinesq approximation for natural convection*, `https://www.comsol.com/blogs/using-the-boussinesq-approximation-for-natural-convection/`.

[11]D. J. Tritton, *Physical fluid dynamics* (Springer Science & Business Media, Netherlands, 2012).

[12]C. Rorres, "Completing book II of Archimedes's on floating bodies", The Mathematical Intelligencer **26**, 32–42 (2004).

[13]B. Woodcroft, "The pneumatics of hero of alexandria", The Pneumatics of Hero of Alexandria Publisher: Taylor Walton and Maberly, London, 1851 (1851).

[14]R Liebe, *Flow phenomena in nature: inspiration, learning and application*, Vol. 2 (WIT press Mulheim, Germany, 2007).

[15]L. Rayleigh, "On the dynamics of revolving fluids", Proceedings of the Royal Society of London. Series A, Containing Papers of a Mathematical and Physical Character **93**, 148–154 (1917).

[16]G. G. Stokes, *On the effect of the internal friction of fluids on the motion of pendulums*, Vol. 9 (Pitt Press Cambridge, 1851).

[17]L Prandtl, "On fluid motions with very small friction", Verhandlungen des dritten internationalen Mathematiker-Kongresses **3**, 484–91 (1904).

[18]L Prandtl, "Entstehung von wirbeln bei wasserströmungen:–1", Entstehung von Wirbeln und Künstliche Beeinflussung der Wirbelbildung. Institut für Wissenschaftlichen Film (DVD)–Historische Filmaufnahmen (1936).

[19]W. Tollmien, H. Schlichting, H. Görtler, and F. W. Riegels, "Entstehung von wirbeln bei wasserströmungen", in *Ludwig prandtl gesammelte abhandlungen: zur angewandten mechanik, hydro- und aerodynamik*, edited by F. W. Riegels (Springer Berlin Heidelberg, Berlin, Heidelberg, 1961), pp. 817–818.

[20]R. J. Kee, M. E. Coltrin, P. Glarborg, and H. Zhu, *Chemically reacting flow: theory, modeling, and simulation* (John Wiley & Sons Hoboken New Jersey, 2017).

[21]T. Linß, *Layer-adapted meshes for reaction-convection-diffusion problems* (Springer-Verlag Berlin Heidelberg, 2009).

[22]W. Rudin et al., *Principles of mathematical analysis*, Vol. 3 (McGraw-hill New York, 1964).

[23]E. S. Oran and J. P. Boris, *Numerical simulation of reactive flow* (Cambridge University Press, 2005).

[24]M. Orban, P. De Kepper, I. R. Epstein, and K. Kustin, "New family of homogeneous chemical oscillators: chlorite-iodate-substrate", Nature **292**, 816–818 (1981).

[25]C. R. Chinake and R. H. Simoyi, "Nonlinear dynamics in chemistry derived from sulfur chemistry. part 2. new experimental data on the chlorite-thiourea reaction", The Journal of Physical Chemistry **97**, 11569–11570 (1993).

[26]I. R. Epstein, K. Kustin, and R. H. Simoyi, "Systematic design of chemical oscillators. 78. kinetics and mechanism of the chlorite-thiourea reaction in acidic medium", The Journal of Physical Chemistry **96**, 5852–5856 (1992).

[27]C. R. Chinake and R. H. Simoyi, "Fingering patterns and other interesting dynamics in the chemical waves generated by the chlorite-thiourea reaction", The Journal of Physical Chemistry **98**, 4012–4019 (1994).

[28]M. A. Budroni, L. A. Riolfo, L. Lemaigre, F. Rossi, M. Rustici, and A. De Wit, "Chemical control of hydrodynamic instabilities in partially miscible two-layer systems", The Journal of Physical Chemistry Letters **5**, 875–881 (2014).

[29]V. Loodts, L. Rongy, and A. De Wit, "Chemical control of dissolution-driven convection in partially miscible systems: theoretical classification", Physical Chemistry Chemical Physics **17**, 29814–29823 (2015).

[30]L. Rongy, P. Assemat, and A. D. Wit, "Marangoni-driven convection around exothermic autocatalytic chemical fronts in free-surface solution layers", Chaos: An Interdisciplinary Journal of Nonlinear Science **22**, 037106 (2012).

[31]R. H. Simoyi, J. Masere, C. Muzimbaranda, M. Manyonda, and S. Dube, "Travelling wave in the chlorite-thiourea reaction", International Journal of Chemical Kinetics **23**, 419–429 (1991).

[32]B. S. Martincigh and R. H. Simoyi, "Pattern formation fueled by dissipation of chemical energy: conclusive evidence for the formation of a convective torus", The Journal of Physical Chemistry A **106**, 482–489 (2002).

[33]B. S. Martincigh, C. R. Chinake, T. Howes, and R. H. Simoyi, "Self-organization with traveling waves: a case for a convective torus", Phys. Rev. E **55**, 7299–7303 (1997).

[34]A. Einstein et al., "On the motion of small particles suspended in liquids at rest required by the molecular-kinetic theory of heat", Annalen der physik **17**, 549–560 (1905).

[35]G. E. Uhlenbeck and L. S. Ornstein, "On the theory of the Brownian motion", Physical review **36**, 823 (1930).

[36]G. Batchelor, "Brownian diffusion of particles with hydrodynamic interaction", Journal of Fluid Mechanics **74**, 1–29 (1976).

[37]J. M. Schurr, "The thermodynamic driving force in mutual diffusion of hard spheres", Chemical Physics **65**, 217–223 (1982).

[38]A. Fick, "V. on liquid diffusion", The London, Edinburgh, and Dublin Philosophical Magazine and Journal of Science **10**, 30–39 (1855).

[39]L. Rongy, G. Schuszter, Z. Sinkó, T. Tóth, D. Horváth, A. Tóth, and A. D. Wit, "Influence of thermal effects on buoyancy-driven convection around autocatalytic chemical fronts propagating horizontally", Chaos: An Interdisciplinary Journal of Nonlinear Science **19**, 023110 (2009).

[40]C. Navier, "Mémoire sur les lois du mouvement des fluides", Mémoires de l'Académie Royale des Sciences de l'Institut de France **6**, 389–416 (1823).

[41]R. Temam, *Navier-stokes equations*, Vol. 2 (Elsevier North-Holland Amsterdam, 1984).

[42]J. H. Ferziger and M. Peric, *Computational methods for fluid dynamics* (Springer-Verlag Berlin Heidelberg, 2012).

[43]R. B. Bird, W. E. Stewart, and E. N. Lightfoot, *Transport phenomena* (John Wiley & Sons New York, 2007).

[44]H. Darcy, *Les fontaines publique de la ville de Dijon*, Vol. 647 (Dalmont, Paris, 1856).

[45]H. C. Brinkman, "A calculation of the viscous force exerted by a flowing fluid on a dense swarm of particles", Flow, Turbulence and Combustion **1**, 27 (1949).

[46]P. G. Drazin and W. H. Reid, *Hydrodynamic stability:* 2nd ed. (Cambridge University Press, Cambridge, Aug. 2004).

[47]P. J. Denning and T. G. Lewis, "Exponential laws of computing growth", Communications of the ACM **60**, 54–65 (2016).

[48]M. T. Heath, A. Ranade, and R. S. Schreiber, *Algorithms for parallel processing*, Vol. 105 (Springer Science & Business Media New York, 1998).

[49]A. Sodani, R. Gramunt, J. Corbal, H.-S. Kim, K. Vinod, S. Chinthamani, S. Hutsell, R. Agarwal, and Y.-C. Liu, "Knights landing: second-generation intel xeon phi product", Ieee micro **36**, 34–46 (2016).

[50]C. R. Chinake and R. H. Simoyi, "Experimental studies of spatial patterns produced by diffusion-convection-reaction systems", J. Chem. Soc., Faraday Trans. **93**, 1345–1350 (1997).

[51]K. Eckert, M. Acker, R. Tadmouri, and V. Pimienta, "Chemo-Marangoni convection driven by an interfacial reaction: pattern formation and kinetics.", Chaos **22**, 037112 –037112–10 (2012).

[52]A. B. Ezersky, A. Garcimartín, H. L. Mancini, and C. Pérez-García, "Spatiotemporal structure of hydrothermal waves in marangoni convection", Phys. Rev. E **48**, 4414–4422 (1993).

[53]L. Šebestíková and M. J. B. Hauser, "Buoyancy-driven convection may switch between reactive states in three-dimensional chemical waves", Phys. Rev. E **85**, 036303 (2012).

[54]M. Gugliotti and T. Silverstein, "Tears of wine", J. Chem. Educ **81**, 67 (2004).

[55]J. D. Ramshaw, "Simple model for linear and nonlinear mixing at unstable fluid interfaces with variable acceleration", Physical Review E **58**, 5834 (1998).

[56]H. G. Lee, K. Kim, and J. Kim, "On the long time simulation of the rayleigh–taylor instability", International journal for numerical methods in engineering **85**, 1633–1647 (2011).

[57]M. Wolfgang, *Flow visualization* (Academic Press (London) LTD, 1987).

[58]T. Bánsági, D. Horváth, A. Tóth, J. Yang, S. Kalliadasis, and A. D. Wit, "Density fingering of an exothermic autocatalytic reaction", Phys. Rev. E **68**, 055301 (2003).

[59]D. Horváth and Á. Tóth, "Diffusion-driven front instabilities in the chlorite–tetrathionate reaction", The Journal of Chemical Physics **108**, 1447–1451 (1998).

[60]C. Thomas, L. Lemaigre, A. Zalts, A. D'Onofrio, and A. De Wit, "Experimental study of co 2 convective dissolution: the effect of color indicators", International Journal of Greenhouse Gas Control **42**, 525–533 (2015).

[61]D. Horváth, T. B. Jr., and Á. Tóth, "Orientation-dependent density fingering in an acidity front", The Journal of Chemical Physics **117**, 4399–4402 (2002).

[62]C. Almarcha, P. M. J. Trevelyan, P. Grosfils, and A. De Wit, "Thermal effects on the diffusive layer convection instability of an exothermic acid-base reaction front", Phys. Rev. E **88**, 033009 (2013).

[63]M. Riaz, G. Kang, Y. Kim, S. Pan, and J. Park, "Efficient image retrieval using adaptive segmentation of hsv color space", in 2008 international conference on computational sciences and its applications (2008), pp. 491–496.

[64]B. H. Gilding and R. Kersner, *Travelling waves in nonlinear diffusion-convection-reaction*, Vol. 60 (Birkhäuser, 2012).

[65]R Kapral and K Showalter, *Chemical patterns and waves* (Springer, Dordrecht, 1995).

[66]S. K. Scott and K. Showalter, "Simple and complex propagating reaction-diffusion fronts", The Journal of Physical Chemistry **96**, 8702–8711 (1992).

[67]J. M. Schurr, B. S. Fujimoto, L. Huynh, and D. T. Chiu, "A theory of macromolecular chemotaxis", The Journal of Physical Chemistry B **117**, 7626–7652 (2013).

[68]J. M. Schurr, "Phenomena associated with gel–water interfaces. analyses and alternatives to the long-range ordered water hypothesis", The Journal of Physical Chemistry B **117**, 7653–7674 (2013).

[69]A. K. Horváth, I. Nagypál, G. Peintler, and I. R. Epstein, "Autocatalysis and self–inhibition: coupled kinetic phenomena in the chlorite–tetrathionate reaction", Journal of the American Chemical Society **126**, PMID: 15149218, 6246–6247 (2004).

[70]A. Indelli, "Kinetic study on the reaction of sodium chlorite with potassium iodide", The Journal of Physical Chemistry **68**, 3027–3031 (1964).

[71]C. R. Chinake and R. H. Simoyi, "Complex reaction dynamics derived from an autocatalytic exothermic chemical reaction.", South African Journal of Chemistry **50**, 220 (1997).

[72]J. Sakakibara and R. J. Adrian, "Measurement of temperature field of a rayleigh-bénard convection using two-color laser-induced fluorescence", Experiments in Fluids **37**, 331–340 (2004).

[73]M. Ciofalo, M. Signorino, and M. Simiano, "Tomographic particle-image velocimetry and thermography in rayleigh-bénard convection using suspended thermochromic liquid crystals and digital image processing", Experiments in Fluids **34**, 156–172 (2003).

[74]K. Eckert, L. Rongy, and A. D. Wit, "A + B → C reaction fronts in Hele-Shaw cells under modulated gravitational acceleration", Phys. Chem. Chem. Phys. **14**, 7337–7345 (2012).

[75]I. Lengyel, L. Gyorgyi, and I. R. Epstein, "Analysis of a model of chlorite-based chaotic chemical oscillators", The Journal of Physical Chemistry **99**, 12804–12808 (1995).

[76]B. S. Martincigh and R. H. Simoyi, "Convective instabilities induced by an exothermic autocatalytic chemical reaction", Phys. Rev. E **52**, 1606–1613 (1995).

[77]G. Csekö, L. Ren, Y. Liu, Q. Gao, and A. K. Horváth, "A new system for studying spatial front instabilities: the supercatalytic chlorite–trithionate reaction", The Journal of Physical Chemistry A **118**, 815–821 (2014).

[78]C. E. Brennen, *Fundamentals of multiphase flow* (Cambridge university press, 2005).

[79]O. Schenk and K. Gärtner, "Solving unsymmetric sparse systems of linear equations with pardiso", Future Generation Computer Systems **20**, 475–487 (2004).

[80]R. L. Street, G. Z. Watters, and J. K. Vennard, *Elementary fluid mechanics* (J. Wiley, 1996).

[81]M. Gulrajani and R Venkatraj, "A low temperature scouring/bleaching process for cotton using sodium chlorite", Textile Research Journal **56**, 476–483 (1986).

[82]V. Loodts, C. Thomas, L. Rongy, and A. De Wit, "Control of convective dissolution by chemical reactions: general classification and application to CO_2 dissolution in reactive aqueous solutions", Physical review letters **113**, 114501 (2014).

[83]J. B. Stock and M. Baker, "Chemotaxis", in *Encyclopedia of microbiology* (Elsevier Inc., 2009), pp. 71–78.